A study of photoneutron spectra around high-energy medical linear accelerators using Monte Carlo simulations and measurements

Robert M. Maglieri

Master of Science

Medical Physics Unit

McGill University

Montreal,Quebec

November 24, 2014

A thesis submitted to McGill University in partial fulfillment of the requirements of the degree of Master of Science in Medical Radiation Physics

ACKNOWLEDGEMENTS

I would like to express my special thanks to my supervisor John Kildea who provided guidance, support and pushed me to really concentrate on my writing. For that I am grateful. I would also like to thank Jan Seuntjens, co-supervisor, and William Parker who gave me the initial opportunity to experience medical physics as a summer student.

Outside the Medical Physics Unit there are many people who made this possible. I would like to thank the Canadian Nuclear Safety Commission for its financial support and initial training; specifically Angel Licea who started me off on the right foot at the beginning of this project. I would also like to thank Jacques Dubeau and Sampath Witharana from Detec who provided excellent technical assistance and knowledge of concepts outside medical physics.

In the Medical Physics Unit many people contributed to the completion of this research project. I have never learned so much in one year of schooling as in Medical Physics. I am grateful for all the instructors and clinical staff for everything they taught me over the years. Particularly, I would like to express special thanks to Stephen Davis who provided knowledge and experience with Monte Carlo simulations.

Last but not least, I would like to thank Melanie who was there in those challenging times and my mother, my father, my sister and my brother for all the moral support.

Thank you all!

ABSTRACT

During high-energy radiotherapy treatments, neutrons are produced in the head of the linac through photonuclear interactions. This has been a concern for many years as photoneutrons contribute to the accepted, yet unwanted, out-of-field doses that pose an iatrogenic risk to patients and an occupational risk to personnel. Presently, in-room neutron measurements are difficult and time-consuming and have traditionally been carried out using Bonner spheres with activation foils and TLDs. In this work, a new detector, the Nested Neutron Spectrometer (NNS) is investigated for use in radiotherapy bunkers. It is designed for easy handling and is more practical than the traditional Bonner spheres providing a quicker and more efficient method to measure neutron spectra. Operated in current mode, the NNS was evaluated around a medical linear accelerator at the Montreal General hospital by: determining the performance, comparing with bubble detectors and comparing with Monte Carlo simulations.

Firstly, the performance of the NNS was evaluated in high dose-rate environments. Reproducibility, linearity and dose-rate tests showed, with coefficient of variation less than 1%, that the NNS consistently reproduced the same raw measured data in each case. Secondly, equivalent doses measured by bubble detectors were compared with those measured by NNS. Absolute differences ranged from 1% in the treatment room to 50% in the maze. Finally, there was good overall agreement between Monte Carlo simulated and NNS measured spectra at various treatment room locations. Spectral characteristics were similar except for a discrepancy in the peak

heights. These tests validate the use of the NNS in radiotherapy.

Additionally, the NNS was used to measure neutron spectra around a new linear accelerator operated in flattening filter free (FFF) mode. Our measurements revealed a decrease in total fluence, neutron source strength and equivalent dose of approximately 35 - 40% across the treatment room for measurements in FFF mode compared with those made in flattening filter mode for the same number of MU.

RÉSUMÉ

En radiothérapie, l'utilisation de photons à haute énergie produit des réactions photonucléaires dans les composantes de l'accélérateur linéaire, ce qui entraine la création de neutrons. Toutefois, ces neutrons exposent le patient à une dose involontaire et augmentent le risque d'absorption de radiation pour le personnel hospitalier. Présentement, la méthode Bonner est utilisée pour mesurer les spectres de neutrons produits lors de la radiothérapie. Cependant, cette technique requiert du temps et plusieurs étapes, puisqu'elle utilise des feuilles d'activation ou des *Thermoluminescent Detectors* (TLD). Un nouveau spectromètre, le *Nested Neutron Spectrometer* (NNS), se distingue toutefois des autres détecteurs de neutrons en raison de sa conception pratique qui permet d'obtenir des données rapidement et efficacement. Il fut donc pertinent d'évaluer le NNS autour d'un accélérateur linéaire à l'Hôpital Général de Montréal, et ce, selon trois méthodes : en établissant sa performance, en comparant la dose équivalente par rapport à celle des détecteurs de bulles ainsi qu'en comparant les spectres avec ceux des simulations Monte Carlo.

Pour ce faire, la performance du NNS a été établie dans une zone de haut débit de dose. L'analyse de la reproductibilité, la linéarité et le débit de dose du NNS ont démontré l'uniformité des mesures avec un écart type de moins de 1%. De plus, la comparaison entre la dose équivalente mesurée par le NNS et par le détecteur de bulles a indiqué des différences de 1% dans la salle de traitement et jusqu'à 50% dans le labyrinthe. Finalement, les mesures des spectres de neutrons du NNS concordaient

avec les simulations Monte Carlo, à l'exception d'un désaccord entre la valeur maximale de leurs sommets.

Enfin, la production de neutrons autour d'un nouvel accélérateur linéaire opéré en mode FFF a été mesurée à l'aide du NNS. Une réduction de 35 à 40 % a été notée dans la salle de traitement entre le mode FFF et le mode conventionnel en ce qui a trait à l'intensité de la source de neutrons et à la dose équivalente.

TABLE OF CONTENTS

LIST OF TABLES

LIST OF FIGURES

CHAPTER 1
Introduction

1.1 Cancer and its Treatment

Every year, approximately 30% of all deaths in Canada are caused by cancer with two in five Canadians developing some form of cancer over the course of their lives[1]. Cancer is a disease, medically termed malignant neoplasm, that begins at the genetic level by a modification of DNA. The cell cycle, which is a series of steps that takes place in a cell leading to its division, determines function, reproduction and death of the cells. The human body contains millions of cells which are always reproducing, sometimes causing deformed cells. Through a repair mechanism, deformed cells can be either repaired or destroyed depending on the complexity of the error. However, the repair process itself sometimes causes an error leading to uncontrolled growth of the cell. The cell reproduces without end creating a mass or tumour that impedes bodily functions and sometimes leads to death. Nevertheless, modern treatments have significantly increased five-year cancer survival rates (over all cancers) from 56% to 63% over the last 20 years[2].

Treatments vary based on cancer type, cancer characteristic, staging and ultimately, patient's wishes. Generally, there are two goals for treatment: cure or palliation. A treatment with a curative intent is designed to cure or control a tumour by removing it and preventing recurrence. Conversely, a palliative treatment is given to relieve symptoms and improve a patient's quality of life when a curative

treatment is not possible. Both curative and palliative intent treatments are achieved through a combination of techniques such as surgery and chemotherapy.

Surgery is the primary method of cancer treatment for isolated solid tumors whereby the cancerous tissue (and a certain margin containing microscopic disease) is removed completely from the body. In many cases, surgery is the only method of treatment for early cancers where the tumour is small and has not spread. When a tumour is too large, chemotherapy or radiotherapy can be used to shrink the tumour to an adequate size for surgery. After a successful surgery, with no further evidence of disease, a patient can be considered "cancer-free".

Unlike surgery, chemotherapy is a minimally-invasive technique that employs cytotoxic drugs to prevent the growth and reproduction of cells. Since cancer cells reproduce quickly, they are most affected by the chemotherapy while healthy tissue is affected to a lesser degree. Chemotherapy can be an effective treatment on its own or used in combination with surgery or radiotherapy. Unfortunately, since these drugs damage rapidly dividing cells, tissues comprising blood, bucal, intestinal and follicle cells are all greatly affected by chemotherapy. This leads to many side effects including bone marrow suppression, sore mouth, nausea, vomiting and hair loss [3].

Surgery and chemotherapy each have their associated benefits and disadvantages with respect to cancer treatment. While it is possible to remove the cancerous tissue completely during surgery, there are risks due to the highly invasive nature of the technique. On the other hand, chemotherapy is minimally-invasive but can cause many negative side effects. There is however another treatment technique that can complement both surgery and chemotherapy: radiotherapy.

1.2 Radiotherapy

Unlike surgery and chemotherapy, most radiation treatments are completely non-invasive. Patients who are unable to undergo surgery or chemotherapy because of their medical condition typically receive radiotherapy. In general, if the treatment has a palliative intent, patients will undergo radiation treatment to relieve symptoms and pain. On the other hand, if the intent is curative then the treatment will most likely be a combination of surgery, chemotherapy and radiotherapy.

Radiotherapy is the use of ionizing radiation to destroy tumour cells while minimally affecting the surrounding normal tissue. Unavoidably, when radiation travels through the body, it will interact with healthy tissue as well as the tumour. The uncontrolled growth of tumors suggests that the majority of its cells lie in the mitotic (M) phase of the cell cycle. This turns out to be the most radio-sensitive. Taking advantage of the growth properties of tumors, two quantities are established in radiation therapy: the tumour control probability (TCP) and the normal tissue complication probability (NTCP). The therapeutic ratio, which is the ratio of these two quantities for a particular radiation dose, relates the tumour response to a certain amount of surrounding normal tissue damage (see Figure 1–1). Ideally, the radiation dose would be given to the tumour in a single treatment to limit patient travel. However, the surrounding normal tissue would not tolerate the whole dose at once. It is instead given to the patient over many treatments, a concept known as fractionation. Over a long period of time, the cells in the tumour respond more than the healthy tissue leading to a larger TCP compared to NTCP. This difference justifies the use of radiation therapy for cancer treatment.

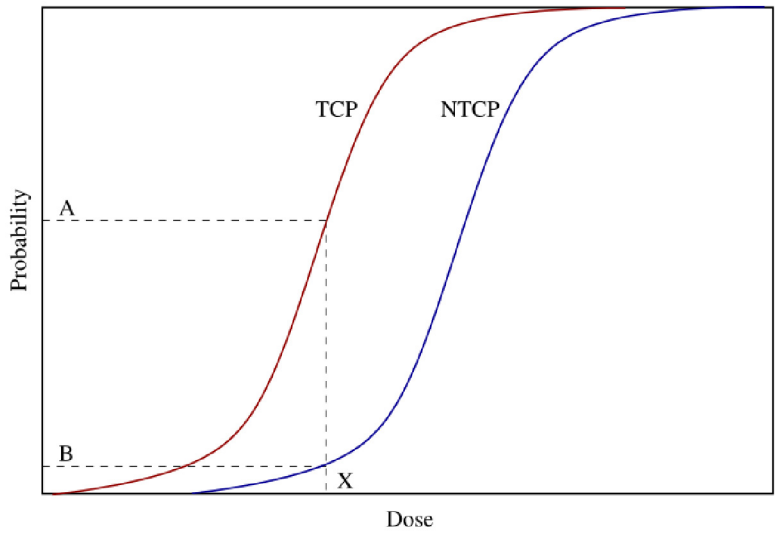

Figure 1–1: Tumor Control Probability and Normal Tissue Complication Probability for a given treatment. For a certain dose X, the therapeutic ratio is A/B. Figure reproduced from Kildea [4]

1.2.1 Radiotherapy Treatment Process

The goal in radiation therapy is to optimize the therapeutic ratio by prescribing a dose of radiation to a region of interest (tumour) while sparing surrounding healthy tissue. The treatment process (see Figure 1–2) begins with a computed tomography (CT) scan to reveal the tumour and organs inside the body. A diagnosis is performed by the radiation oncologist who then outlines the tumour and organs at risk on the CT scan. Following a dose prescribed by the oncologist, a treatment plan is simulated by dosimetrists. After the plan is approved by the radiation oncologist and a medical physicist, radiation therapists set up the patient in the same position as the initial CT scan and deliver the treatment. Positional accuracy is essential to ensure that the tumour (and healthy tissue) receives the correct radiation dose.

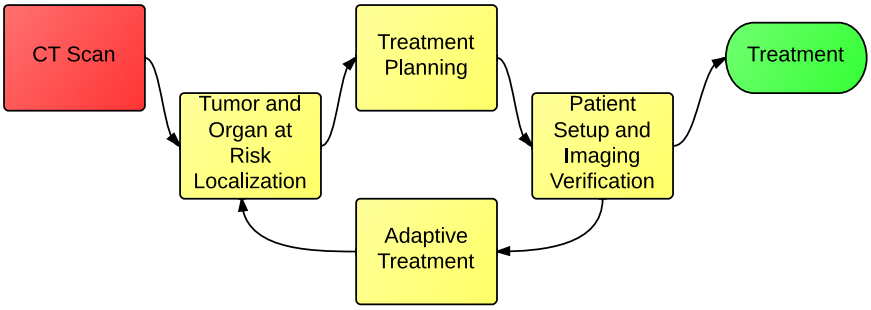

Figure 1–2: The radiotherapy treatment process.

While straightforward, this process is dependent on a very precise radiation delivery system which is the responsibility of the medical physicist.

There are two common radiation delivery techniques in radiotherapy: external beam radiotherapy and brachytherapy. External beam radiotherapy, defined as radiation delivery from a source that is exterior to the body, is the most common technique, accounting for 80 % of all radiation treatments. Unlike external beam, brachytherapy is the administration of radiation by temporarily or permanently implanting a source into the tumour allowing for greater sparing of healthy tissue. Ultimately, the choice of treatment depends on the location, size, and type of tumour as well as patient health.

1.2.2 External Beam Radiotherapy

Depending on the tumour, different types of external beam radiotherapy are used for treatment. Conventional 3D conformal, which involves the intersection of one

or more conformal shaped beams at the tumour, and Intensity Modulated Radiation Therapy (IMRT), which applies many intensity modulated beams using inverse treatment planning, are among the many external beam modalities. Once a treatment technique has been chosen, the absorbed dose, defined as the energy absorbed per unit mass (J/kg), is simulated at the regions of interest in the patient's body based on calculations of the interaction of radiation with tissue[1] .

To simulate radiation interactions, the patient's body is assumed to be water. As radiation enters a medium (in this case water), the absorbed dose decreases with depth (except heavy charged particles which deposit their energy in a single peak called the Bragg peak). This can be described by a quantity known as the percent depth dose (PDD). The percent depth dose at a particular depth is defined as the absorbed dose at that depth normalized to the maximum as shown in Figure 1–3. Dependent on particle type, energy and absorbing medium, the characteristics of a PDD will change. This provides a basis for selecting a suitable treatment modality for a given tumour. For superficial tumors, orthovoltage x-ray units, with shallow depth dose curves, deliver radiation with energies ranging from 10 keV to 500 keV. Conversely, for deep seated tumors, linear accelerators deliver high-energy radiation ranging from 2 MV to 25 MV. Inevitably, while gaining the ability to reach deeper into the body, more healthy tissue is also irradiated.

[1] Many modern dose calculation algorithms assume a patient is completely comprised of water of varying densities.

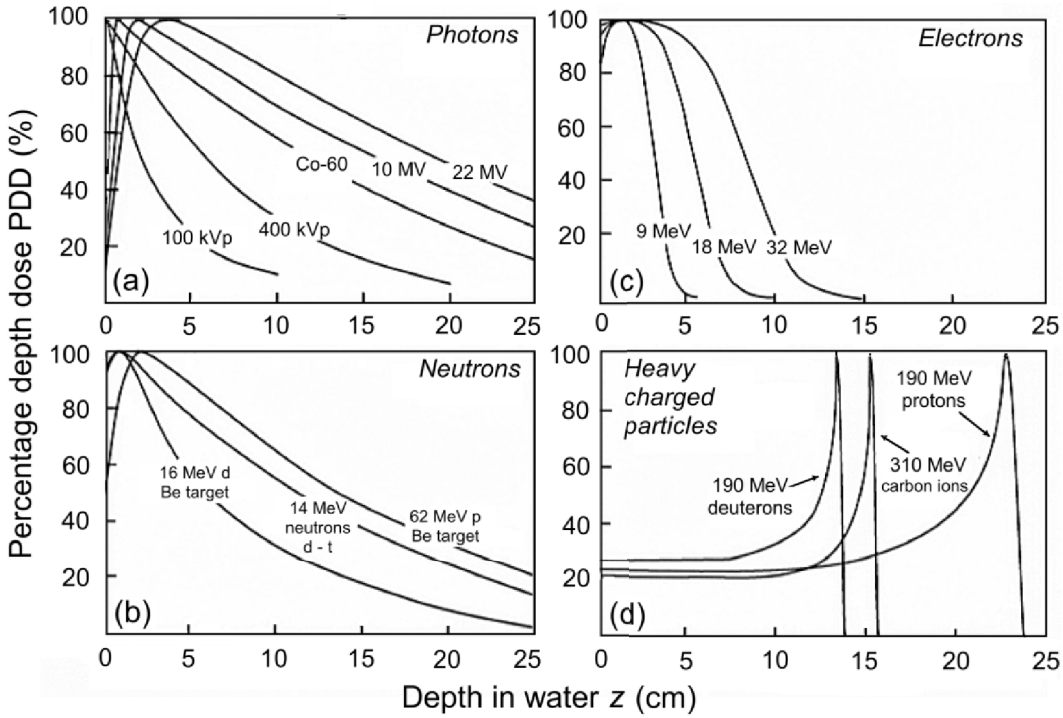

Figure 1–3: Percent Depth Dose curves in water for different particles. (a) photons, (b) neutrons, (c) electrons and (d) protons and heavy charged particles. The prescribed dose in an external beam treatment is delivered via a clever manipulation of these curves [5]

1.3 Radiation Protection in Radiotherapy

While radiation is beneficial for the treatment of cancer, it can still be dangerous for the patient, the hospital personnel as well as the members of the public in areas surrounding the treatment suites. At large doses, radiation can cause acute effects such as intestinal failure, blood cell loss and, in extreme cases of irradiation, death. At low doses radiation may be carcinogenic. Therefore, it is important to take all the necessary precautions before installing any radiation emitting equipment.

The subfield of physics that deals with health and safety pertaining to ionizing radiation is health physics. The findings of health physics guide the creation of radiation safety regulations. Since there is a non-zero risk associated with the use of radiation, the goal in health physics and radiation protection is to minimize the risk while maintaining the benefits of radiation use.

1.3.1 Basic Physics of Radiation Protection

Health physicists have based radiation protection on three underlying tenets: distance, time and shielding [6].

- **Distance**: Dose rate emitted from a point source decreases as a function of the distance squared; increasing the distance from the source will significantly decrease the amount of radiation received.
- **Time**: Radiation dose is cumulative. The time of exposure should be minimized.

- **Shielding**: When there is no longer the option to increase distance or minimize time, an effective shield should be positioned in front of the source. Any material will attenuate a radiation beam as a function of its thickness, composition and the characteristics of the radiation itself.

These basic tenets allow a physicist to evaluate, design and build an effective radiation protection program.

1.3.2 The ALARA Principle

As radiation absorbed dose accumulates in humans, there is believed to be a linearly increasing (no threshold) probability that it will cause long-term effects such as cancer. This is known as the *linear-no-threshold* (LNT) model and is largely a result of extrapolated data observed at higher doses from the bombings in Hiroshima and Nagasaki[6]. While the extrapolation leads to large uncertainties at low doses, the LNT model is a good conservative estimate for radiation protection.

As a direct manifestation of the LNT model, one of the main goals in radiation protection is to keep absorbed doses as low as reasonably achievable (ALARA). The ALARA principle stipulates that radiation exposure levels should not simply respect the limits set by regulatory bodies, but should also be minimized as much as possible, social and economic factors taken into account.

1.3.3 Quantities of Interest

The ALARA principle relies on the accurate quantification of radiation known as radiation dosimetry. In health physics, there are two main quantities that measure the quantity and effect of radiation: equivalent and effective dose. The equivalent dose allows us to account for the relative biological effect for carcinogenesis of different

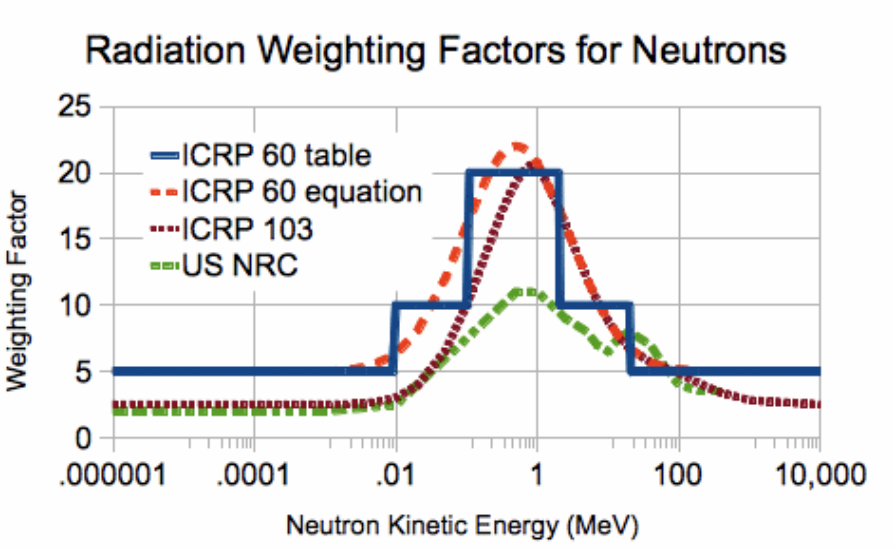

Figure 1–4: Neutron weighting factors for different publications. The neutron weight can reach up to a factor of 20 around 1 MeV. Figure reproduced from Wikipedia. See ICRP 103 for details[6].

radiation types by multiplying the absorbed dose with weighting factors w_R specific to radiation type. For example, at certain energies neutron weighting factors can reach up to 20 as shown in Figure 1–4.

The effective dose accounts for the radiation damage based on tissue type. Every organ has its own weighting factor which is multiplied by the equivalent dose. This enables us to calculate individual organ doses or total whole body doses accounting for the effects of radiation and organ type.

1.4 Scope of Thesis

Neutron production as a result of photonuclear interactions [2] in linear accelerators have been an unwanted by-product of radiotherapy treatments since high-energy photon beams first started appearing in the 1950s. Compared to photons, neutrons can produce carcinogenic mutations up to twenty times more effectively and contribute additional dose to the patient during treatment. Although the number of neutrons produced in a medical linear accelerator is relatively low compared to the photon flux, there are health concerns about using photon energies capable of producing photoneutrons. One way to mitigate this risk is to install shielding that will absorb neutrons.

Prior to installing additional shielding around a linear accelerator, photoneutron production should be quantified. There are many methods to measure neutron spectra including nuclear recoil, velocity measurements, threshold methods and multisphere measurements[7]. In radiotherapy, the most common technique is to make use of the multisphere method with an energy range from 10^{-8} to 200 MeV. The multi or Bonner sphere (BS) technique makes use of a central thermal neutron detector surrounded by different sized spheres of hydrogenous material (moderators). The purpose of each moderator is to decrease the incident neutron energy such that it can interact in the detector.

[2] Photons are absorbed by a nucleus which then ejects a neutron. More details in the following chapter.

Traditionally, passive neutron detectors such as gold activation foils [8] and thermoluminescent detectors [9] have been used in conjunction with Bonner spheres[10] to measure neutron spectra in radiotherapy. While these methods generally provide good results, they often require a long setup time and a large storage space owing to the large number of spheres. In addition, passive detectors require an additional step to 'readout' data after the experiment, further increasing the overall measurement time.

Recently, a new type of neutron detector, the Nested Neutron Spectrometer (NNS) [11], has appeared on the market. The NNS is uniquely designed for easy handling and storage, improving the traditional Bonner sphere design. Instead of manipulating 3-12 very large spheres, the NSS varies cylindrical moderators in a Russian doll fashion for ease of use cutting down on measurement time and allowing it to be stored in a smaller space. Furthermore, the NNS can be operated in two modes: pulse and current mode. In pulsed mode, it is used to detect neutrons in low dose rate areas. In current mode, the NNS can be used to detect neutrons in high dose-rate environments. As such, the NNS presents itself as a suitable replacement for the Bonner sphere system.

In this thesis, a feasibility study is carried out to evaluate the use of the NNS as a new spectrometer to measure neutron spectra in high dose-rate environments such as radiotherapy treatment rooms. Chapter 2 presents the radiation interactions, measurement techniques and simulation methods of importance for neutrons. Chapter 3 describes the setup and results of Monte Carlo simulations calculating

neutron production for comparison with the NNS. Chapters 4 and 5 detail the procedure to validate the use of the NNS in radiotherapy environments and describe measurements around a linear accelerator operated in a new "flattening-filter-free" treatment mode. Finally, the conclusions of this project are summarized in Chapter 6.

CHAPTER 2
Radiation Interactions, Measurement and Simulation

2.1 Radiation

The word radiation originates from the Latin verb *radiare*, which means to emit rays. In physics, radiation is defined as the emission of energy from a source. This energy travels through space with or without the presence of media. Light, heat and sound are examples of radiation.

2.2 Ionization: Categorizing Radiation

Under normal conditions, an atom or molecule is neutral; the number of electrons is equal to the number of protons. When a bound electron acquires enough energy to overcome the electromagnetic force of the nucleus, it can be ejected from the atom leaving a hole, a process known as ionization. The atom now contains one less electron and is termed an ion.

Ionizations are produced via photon interactions (Compton effect, photoelectric effect and triplet production), electronic reconfigurations (Auger effect, electron capture and internal conversion) and charged particle interactions (Coulomb scattering and positron annihilation). Ionization can also be used to categorize radiation as either ionizing or non-ionizing. Non-ionizing radiation does not carry enough energy to ionize an atom or molecule. Certain ultraviolet rays, visible light, infrared light, microwave and radio waves are non-ionizing. On the other hand, electromagnetic waves or sub-atomic particles with enough energy to eject electrons from atoms or

molecules are termed ionizing. These include gamma rays, x-rays, electrons, neutrons and heavy charged particles.

In an atom or molecule, the electromagnetic force is quantized with respect to each atomic shell; the energy required to ionize an atom, or binding energy, is thus also quantized. While each electron has its own binding energy, the lowest energy required to ionize an atom is termed the ionization potential. Noble gases, being the most stable elements, have the highest ionization potentials while alkali elements, the least stable elements, have the lowest ionization potentials.

2.3 Radiation Interactions with Matter

2.3.1 Charged Particle Interactions

A neutral particle entering a medium deposits its energy in a two-step process. Energy is initially transfered to a charged particle that then deposits the energy locally. As this charged particle travels through matter it undergoes Coulomb interactions with the absorber atoms described through three distinct processes: soft collisions, hard collisions and radiative events (shown in Figure 2–1). These processes are governed by two important parameters: the impact parameter b and the atomic radius a.

When b is on the order of a, a hard collision occurs; a charged particle will interact with an orbital electron of the atom transferring a large amount of its energy. The orbital electron will leave the atom as a δ ray and undergo its own Coulomb interactions.

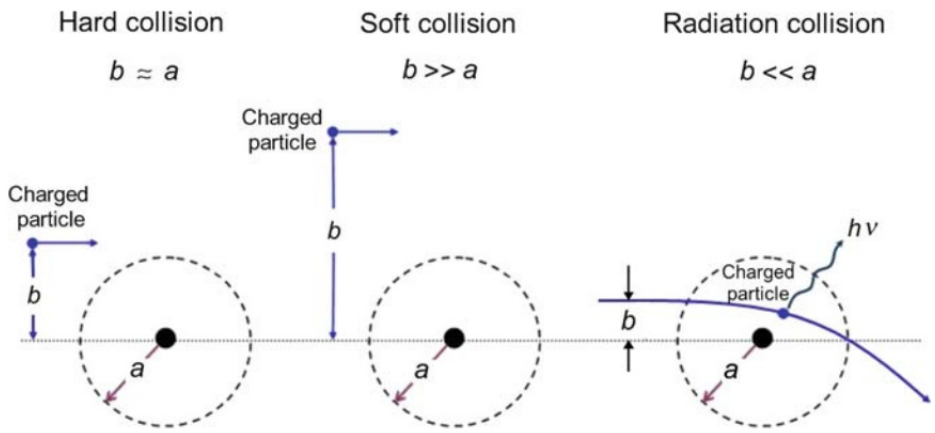

Figure 2–1: The different charged particle interactions with matter. $b \approx a$ results in a hard collision, $b >> a$ a soft collision and $b << a$ a radiative (bremsstrahlung) interaction.[5]

When $b >> a$, the charged particle interacts with the atom as a whole, resulting in a soft collision. Compared to hard collisions, the Coulomb force is much weaker, causing ionizations or excitations.

Finally, when $b << a$, the charged particle interacts with the external electromagnetic field of the nucleus. A deceleration causes part of the charged particle's kinetic energy to be emitted in the form of bremsstrahlung photons in a process termed radiative loss.

Linear accelerators produce photon beams by bombarding high-Z (materials with large atomic number Z) targets with electrons. As an electron hits the target, most of the energy is transformed into heat. However, in some cases the interaction will result in radiative loss producing photons. These photons make up the clinical photon beams that are used in radiotherapy treatments.

2.3.2 Radiation Beam Attenuation

A monoenergetic radiation beam entering a medium is attenuated through particle interactions with the medium. Each interaction has its own probability or cross section σ as a function of the particle's energy. The larger the cross section, the more prominent the interaction type. The sum of all the different cross sections multiplied by the atom density N will determine the total probability of interaction in a material. This is known as the total macroscopic cross section Σ_t.

Given the total macroscopic cross section and the depth x in the medium, the intensity $I(x)$ of a radiation beam at a depth x can be described by the Beer-Lambert law of attenuation as follows

$$I(x) = I_0 e^{-N\sigma_t x} \tag{2.1}$$

where x is the depth in the material, $\Sigma_t = N\sigma_t$ is the macroscopic cross section and I_0 is the initial beam intensity.

At the energies of interest in radiotherapy, 2-25 MV, many different photon interactions impact on the macroscopic cross section (termed linear attenuation coefficient for photons). Compton scattering, photoelectric effect, pair production and photonuclear reactions all contribute significantly to the linear attenuation coefficient. In the context of this thesis, only photonuclear interactions will be discussed in detail.

2.3.3 Neutron Production in External Beam Radiotherapy

In external beam radiotherapy, therapeutic photon beams are produced by medical linear accelerators. These beams are generated by accelerating mono-energetic electrons toward a target. The interaction of electrons with the target material causes them to decelerate and produce bremsstrahlung photons. This results in a beam of photons that can be shaped to a tumor by various collimators.

At photon energies above ∼7 MV, neutrons can be produced through interactions with materials in the linear accelerator in a process known as photoneutron production. This process can only occur if the incident photon energy is greater than the threshold energy of the (γ,n) reaction. Thresholds are unique to each element and are calculated from the Q-value[1] of the photonuclear reaction (see Table 2–1).

Photoneutron production is a specific interaction of the more general photodisintegration. Photodisintegration is the interaction between a high energy photon and the nucleus of an absorber which can lead to the production of neutrons (γ,n), (γ,2n), protons (γ,p), alpha particles (γ,α) and a combination of these (γ,np), (γ,nα).

At the energies of interest in radiotherapy, the cross section for photoneutron production results from the weighted cross sections of two different processes: photoionization and compound nucleus formation. The photionization process is the process in which all of the photon energy is transferred to the neutron. Neutron spectra are thus obtained from a combination of the bremsstrahlung spectrum and

[1] The Q-value is the energy required or released for the nuclear reaction to occur.

Table 2–1: Threshold energies for photonuclear production of the elements present in a typical medical linear accelerator. Data from IAEA photonuclear handbook[12]

Element	Threshold [MeV]
Tungsten-184	7.41
Copper-63	10.85
Iron-56	11.2
Tantalum-181	7.58
Lead-207	6.74

the photoionization cross section. This is the main neutron production process for light nuclei, while it only accounts for 10-20% in heavy nuclei [13].

The compound nucleus formation, on the other hand, is the main contributor to the photoneutron production cross section for nuclei with atomic weights greater than 40. This is a photon evaporation process that produces a spectrum of neutron energies irrespective of incident photon energy around the threshold energy. At large atomic weights, this spectrum peaks around 1 MeV.

Both these processes produce a spectrum of neutron energies. By combining the two processes for the many shielding materials present around a medical linear accelerator, a blurred out single peak neutron spectrum is expected. However, in a radiotherapy treatment room, the walls will moderate the fast neutrons to lower energies resulting in a neutron spectrum spanning thermal to fast neutron energies. An example neutron spectrum at 50 cm from the isocentre of a radiotherapy bunker is shown in Figure 2–2.

In radiotherapy, photonuclear reactions account for less than one percent of the total photon cross section. However, photoneutrons are far more penetrating

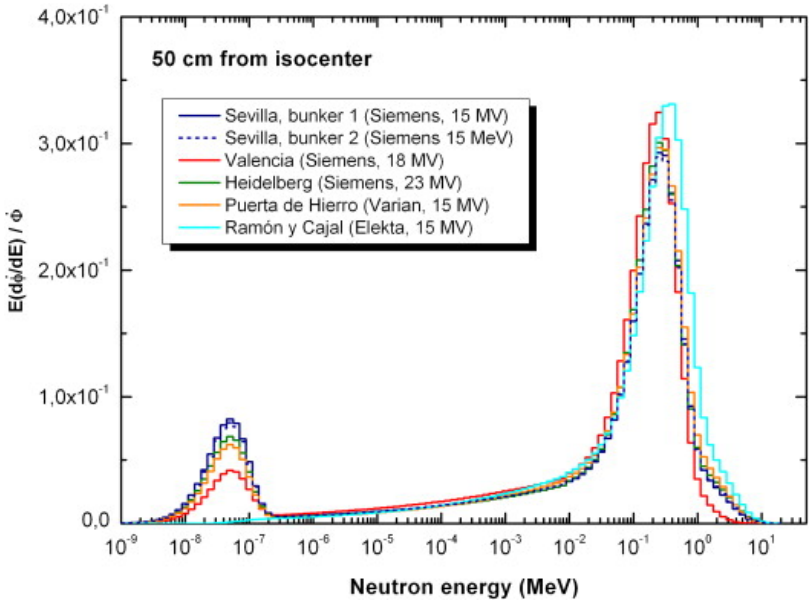

Figure 2–2: Neutron spectrum at 50 cm from the isocentre for various linear accelerators and treatment rooms. Figure reproduced from Domingo[14]

compared to the initial photons that produced them. Along with other sources of radiation, neutrons must always be considered and adequately shielded.

2.4 Neutrons

2.4.1 Classifying Neutrons

In thermal equilibrium at room temperature, the most probable neutron energy given by the Maxwell-Boltzmann distribution is 0.025 eV. Neutrons at these energies are known as *thermal* neutrons. Using this as a reference, neutrons are classified based on kinetic energy, E_k. There are many variations to the naming convention for neutrons, however, in this research project, neutrons are classified in the following manner[5]:

1. Cold neutrons: $E_K < 0.025$ eV

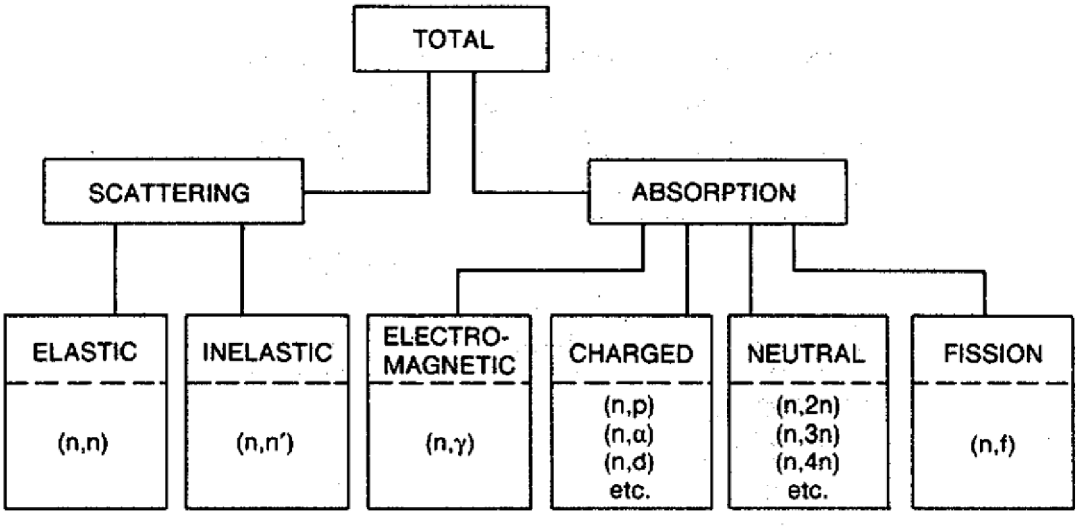

Figure 2–3: Various categories of neutron interactions. Absorption is also termed neutron capture. The main interactions of concern in medical physics are elastic and inelastic scattering and charged and electromagnetic absorption. [15]

2. Thermal neutrons: $E_K \approx 0.025$ eV
3. Epithermal neutrons: $0.025 \text{ eV} < E_K < 1$ keV
4. Intermediate neutrons: $1 \text{ keV} < E_K < 0.1$ MeV
5. Fast neutrons: $E_K > 0.1$ MeV

A number of different interactions are available to the neutron based on its kinetic energy (see Figure 2–3). In the energies important to radiotherapy, 0.025 eV to 25 MeV, elastic and inelastic scattering as well as neutron capture (absorption) are the most common. A graphical overview of the most probable interactions with respect to neutron temperature is shown in Figure 2–4.

2.4.2 Elastic Scattering

Elastic scattering occurs when a neutron of mass m_1, incident on a nucleus of mass m_2 recoiling with angle ϕ, scatters at an angle θ as shown in Figure 2–5. As with

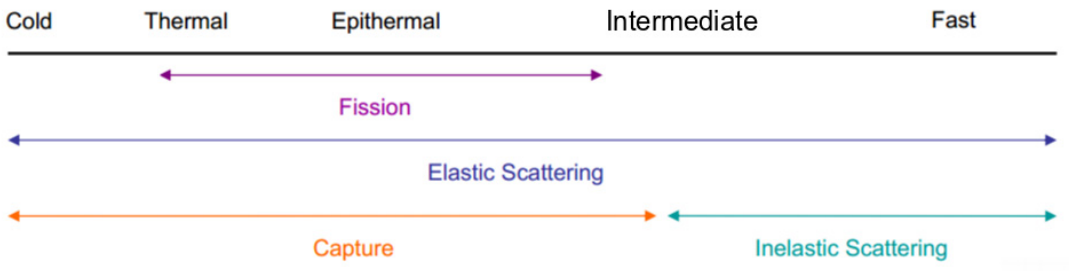

Figure 2–4: Prominent interactions based on neutron energy. Figure adapted from a presentation by Dr. David Hamilton.[16]

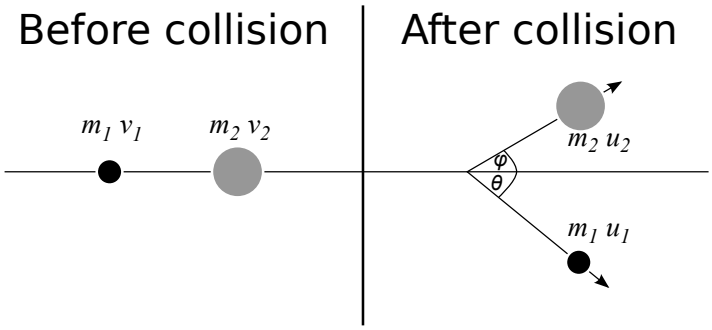

Figure 2–5: Diagram of an elastic collision between an incident projectile and a stationary target ($v_2 = 0$). The projectile is scattered with angle θ and nucleus with angle ϕ.[5]

many scattering interactions, there is a maximum possible energy transfer that occurs in a head on collision at $\phi = 0°$. Mathematically, this is described as

$$(\Delta E_K)_{max} = (E_K)_{initial} \frac{4m_1 m_2}{(m_1 + m_2)^2} \tag{2.2}$$

On average, the kinetic energy transferred to the recoil nucleus is $\frac{1}{2}(\Delta E_K)_{max}$. Thus, for example, if the target nucleus is hydrogen, then $m_2 = m_p \approx m_n$ and the average energy transfer to the proton is about half the initial kinetic energy of the neutron,

while the maximum energy transfer is almost the entire kinetic energy of the initial neutron. The protons resulting from these interactions quickly lose their energy via Coulomb interactions, depositing it locally. Therefore adding hydrogen-rich materials to treatment rooms can significantly decrease the presence of neutrons. If, on the other hand, m_2 increases (increasing atomic number), the energy transfer becomes much less efficient. For example, in a lead nucleus there is 2% fractional energy transfer between the impinging neutron and the nucleus on average.

2.4.3 Inelastic Scattering

When the energy of the neutron is high enough, inelastic scattering with nuclei can occur. The nucleus undergoes an internal rearrangement into an excited state and is de-excited by emitting high energy gammas. The energy of the scattered neutron is less than the incident neutron's since part of the energy is transferred to the nucleus. Mathematically, it is no longer trivial to calculate the average energy loss of the neutron since it will depend on the energy levels in the nucleus.

2.4.4 Neutron Capture (Absorption)

Neutron capture is the result of a thermal neutron interacting with a nucleus. The neutron is absorbed followed by one of a variety of emissions as shown in Figure 2–3. These include the emission of one or more gammas following an internal rearrangement of the nucleus, the emission of charged particles such as protons, deuterons or alpha particles, the emission of neutrons which are indistinguishable from single neutron emissions or finally, the emission of fission fragments after a fission event.

2.5 Measurement and Detection of Radiation

Radiation detectors are used to detect and quantify radiation by producing a signal that is proportional to the energy of the radiation traveling through them. The signal produced will vary depending on the particle, the interaction and the detector medium.

There are generally two types of detectors: particle detectors and radiation dosimeters. Particle detectors measure the effect of ionizing particles traveling through the detection medium, whereas radiation dosimeters produce a signal that is proportional to the dose that is absorbed in the detection medium. For radiation safety, radiation detectors and dosimeters are used in many different scenarios: area monitoring, personal exposure monitoring, calibrations, dosimetry, contamination measurements and many others.

In this research project, two detectors were used to measure neutron spectra and dose: a gas-filled neutron spectrometer and bubble detectors. These are described in detail below.

2.5.1 Gas-Filled Detectors

A gas-filled detector is used to detect the presence of radiation by quantifying ionizations produced inside a gas. In the presence of an electric field, the resulting ions are attracted to electrodes surrounding the gas. This produces a measurable charge collected by a circuit known as a leaky-capacitor circuit (see Figure 2–6). The charge is processed through various amplifiers and filters and can be related to the energy deposited in the detector.

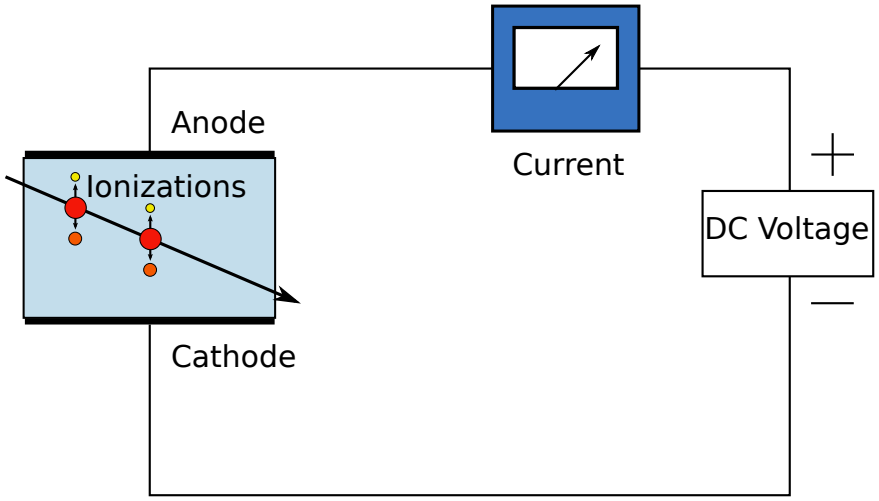

Figure 2–6: Simplified schematic design of a typical gas-filled detector.

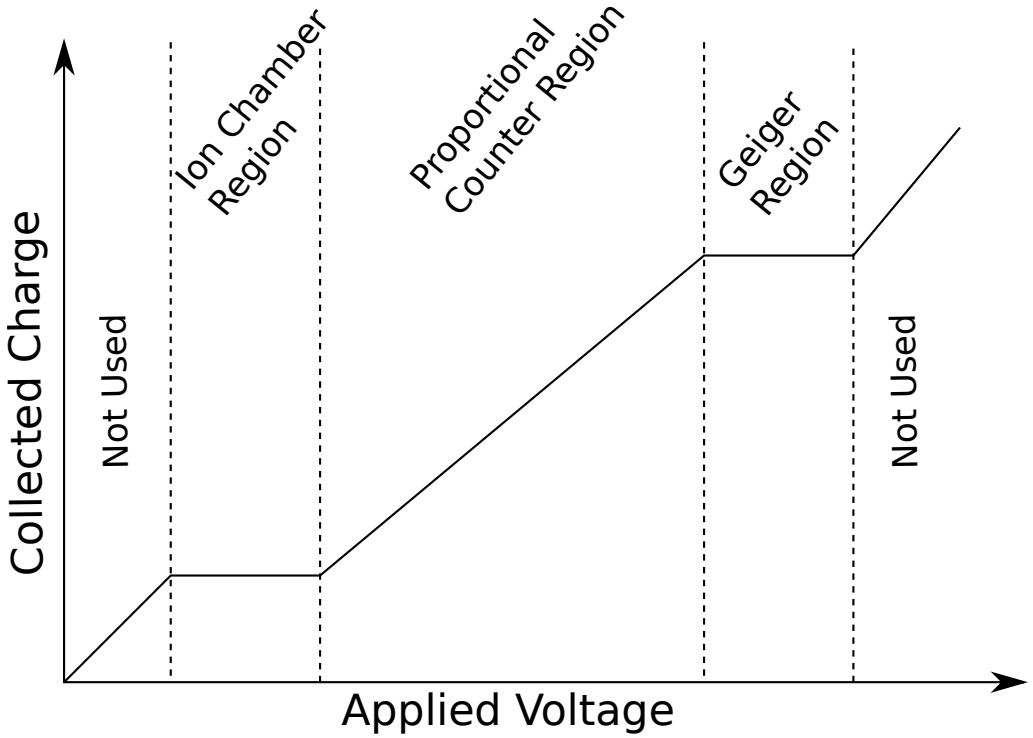

Figure 2–7: Relationship between the output signal and applied voltage in a gas-filled detector for a given charge deposition. The first and last (from left to right) are unsuitable for dosimetry and spectroscopy.

Gas-filled detector response varies widely based on the voltage applied to the electrodes as shown in Figure 2–7. At low voltages, the electric field is not sufficient to overcome the effects of ion recombination. On the other hand, at high voltages, a single ionization may induce a continuous avalanche making the signal unstable. Between these two extremes lie the ionization chamber, proportional counter and Geiger-Mueller regions. These three commonly used regions are described below.

Ionization Chambers

Compared to proportional counters and Geiger-Mueller counters, ionization chambers make use of the lowest voltages. These low voltages create an electric field in the gas that can overcome ion-recombination. As a result, every ionization creates an ion pair[2] that is collected in the electrodes. With a known W-value[3] for the gas, the number of ion pairs produced can be related to the energy deposited.

Given that the electrical signal for a single particle is low relative to the noise and leakage in the detector, single event detection is not possible. Therefore, in most applications, ionization chambers are used to measure cumulated charge over a certain time. This allows the low signal of each individual ionization to be integrated over the time interval to produce a current. With this current (and charge), it is possible to obtain dose rates (and total dose) for a given irradiation.

---

[2] An ionized molecule and its associated free electron are known as an ion pair.

[3] W-value is the average energy required incident particle to create an ion pair.

Proportional Counters

Unlike ionization chambers, proportional counters are designed to count single pulses or events where the signal is proportional to the to the energy deposited by the radiation. In the proportional counter region of Figure 2–7, larger signals are observed as the voltage to the electrodes increases. These large signals are not a result of the voltage directly, but of a phenomenom known as charge multiplication. As ionizing radiation enters the sensitive volume of the detector, it produces an ion pair. The positive ion drifts towards the cathode while the electron drifts towards the anode. This drift region acts as an ion chamber with an electric field large enough to prevent recombination. As the electron approaches the anode wire, there is a large increase in electric field strength that causes Towsend avalanches[17]. This occurs when a free electron, accelerated by a large electric field, gains enough energy to produce ionizations as it interacts with neutral molecules. Electrons released by this process are also accelerated and can, in turn, produce more ionizations. As a result, every ionization event in a proportional counter has an avalanche associated with it. This produces a large signal in the detector making it ideal for the measurement of single events.

Geiger-Mueller Counters

Compared to proportional counters, Geiger-Mueller counters also experience gas multiplication but to a much larger degree. After ionization, the high voltage causes secondary particles to produce excitations in other molecules. These excitations are large enough to be de-excited by the emission of a UV photon. The UV ray then creates additional ionizations and avalanches at different locations in the detector. The

number of avalanches increases exponentially until the concentration of ions begins to reduce the electric field in the gas, terminating the chain reaction. The number of ions needed to halt the reaction is fairly constant resulting in the same electric signal amplitude for each initial event. Given the large constant signals produced in the detector, Geiger-Mueller counters are best used to detect individual ionization events irrespective of energy or particle type.

Pulse and Current Mode of Detection

There are two common methods of operation for gas-filled detectors: pulse-mode and current-mode. In pulse-mode, the detector electronics are designed to produce a signal that preserves the amplitude and timing of charge pulses[4] . The amplitude and timing provide information about the energy deposited and the rate of detection in the detector. One disadvantage is that pulse-mode detectors suffer from electronic limitations when the count rate is large. This large number of pulses can pile up in the detector and paralyze it. Consequently, pulse-mode detectors are mainly suitable for situations where the event rates are low.

In current-mode, the total charge is collected and integrated over a time interval and the problem of paralyzability disappears. This allows current-mode detectors to operate in high event-rate environments. As such, the downside to current-mode is the impossibility of distinguishing individual events. Consequently, current-mode is

[4] A charge pulse is an electrical signal (voltage, current or charge) that is collected in the electrodes of the detector as a function of time.

suitable when event rates are high and the ability to discriminate events is unimportant.

Neutron Spectroscopy

As discussed in Chapter 1, the energy of a neutron has an effect on the equivalent dose that it deposits in tissue. At low energies, neutron weighting factors are approximately two times greater than those of photons. However, for energies around 1 MeV, weighting factors rise to ∼20. Thus it is important to measure the entire spectrum of neutron energies in order to obtain an accurate equivalent dose.

Neutron spectroscopy is defined as the quantitative study of the energy spectra of a neutron field. Most detectors used to measure neutron spectra are operated in pulse-mode. However, in this study, we made use of a technique that operates a detector in current-mode (see Chapter 4) to sample a photoneutron spectrum around a medical linear accelerator. Using current-mode allowed us to quantify the neutron fluence in the high-dose rate environment of the pulsed-beam linac.

2.5.2 Neutron Detection

Since neutron energy determines the interaction type, neutron detectors are classified in two categories, slow and fast neutron detectors.

Slow Neutron Detection

A slow neutron detector measures the signal resulting from a thermal neutron causing a nuclear reaction within a gas. In a thermal neutron interaction, the energy of the incoming neutron (∼0.025 eV) is much smaller than the Q-value of the reaction; the energy imparted to the products from the thermal neutron is thus negligible,

resulting in a gain of energy by the products equal to the Q-value. As a result, the signal produced in the detector is essentially the Q-value.

Three common elements are used as detection media because of their high Q-values for neutron interactions: ^{10}B(n,α)^{7}Li with Q-values of 2.792 MeV and 2.310 MeV[5] , ^{6}Li(n,α)^{3}H with Q-value of 4.78 MeV and ^{3}He(n,p)^{3}H with Q-value of 0.764 MeV. Even though He-3 has a lower Q-value than B-10 and Li-6, its thermal neutron cross section (see Figure 2–8) is much larger: 5330 barns for He-3, 3840 barns for B-10 and 940 barns for Li-6. Consequently, He-3 is a common choice of detection medium for slow neutron detectors.

A major consideration for the development of slow neutron detectors is the ability to discriminate neutrons from gammas. A photon with energy similar to the Q-value will produce an electron via Compton scattering or pair production with a certain range. Compared to the range of ions produced from the nuclear reaction, the electron range is much greater; only a minimal amount of energy will be deposited in the gas as ionizations. To maximize this difference, gases with higher Q-values can be selected.

Fast Neutron Detection by Moderation

In principle, B-10, Li-6 and He-3 can also be used to detect fast neutrons. However, as shown in Figure 2–8, the He-3 cross section decreases with the kinetic energy of the impinging neutron. This also applies to the other elements and has a drastic effect on

[5] Q=2.792 MeV is the excited stated of Li while Q=2.310 MeV is the ground state after release of a 0.48 MeV gamma.

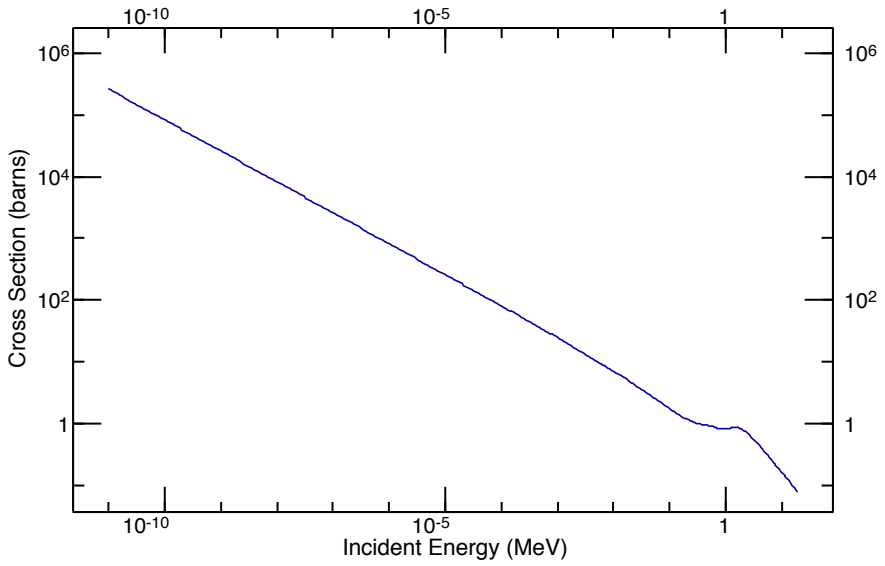

Figure 2–8: Cross section of the (n,p) reaction for He-3. There is an inverse energy dependence. Data in Evaluated Nuclear Data File (ENDF)

the detection efficiency. One way to overcome this is by introducing a hydrogen-rich material surrounding the thermal detector to decrease, or *moderate*, the energy of the fast neutrons. By doing so, the neutron energy is decreased such that interaction in the gas is more likely. A schematic description of neutrons slowing down inside a moderator is shown in Figure 2–9.

The first fast neutron spectrometers were developed by T. W. Bonner[10] in the 1960s. They Bonner system consists of seven spherical moderators with varying diameters and an internal lithium iodide scintillator. Each sphere has a specific response to a reference neutron spectrum: the largest moderators make the detector sensitive to the highest energies while the smallest make the detector most sensitive to the lowest energies. By measuring the neutron count rate with each sphere in place, an unfolding algorithm may be used to deconvolve the measurements of each

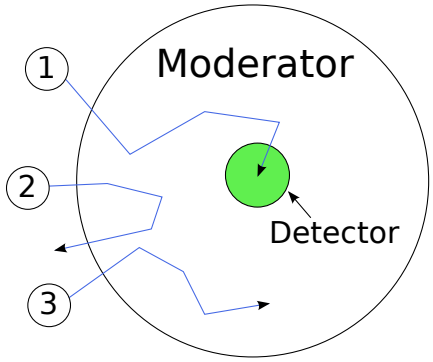

Figure 2–9: Neutrons inside a moderator. Neutrons labeled 1 are moderated and detected. Neutrons labeled 2 are moderated but escape. Neutrons labeled 3 are absorbed by the moderator.

moderator into a full spectrum (Section 2.5.5). This method is one of the most commonly-used to measure neutron spectra and is an active area of research.

2.5.3 Bubble Detectors

Unlike gas-filled detectors which require sensitive electronics to acquire a signal, bubble detectors are passive integrating neutron dosimeters that measure equivalent dose. Inside a glass tube, thousands of superheated liquid droplets are suspended in a polymer and are vaporised when struck by neutrons (see Figure 2–10) producing clearly visible bubbles that are readily counted, and whose number is proportional to cumulative equivalent dose. The bubbles are counted by eye with the help of software to keep track of the already counted bubbles (Reference F. DeBlois, private communication).

Bubble detectors supplied by Bubble Technology Industries (BTI) are fully temperature-compensated, have zero sensitivity to gamma radiation and are reusable. Through a compression of the gel the detectors can be re-used many times. In this

Figure 2–10: Bubble Detectors. The upper glass tube contains a polymer with superheated droplets that produce bubbles when struck by neutrons as in the lower tube. Figure reproduced from BTI bubble detector data sheet.

work, the bubble detectors were calibrated by the manufacturer using an AmBe reference neutron source.

2.5.4 Nested Neutron Spectrometer

The Nested Neutron Spectrometer (NNS) is a neutron spectrometer comprising a gas-filled He-3 detector sensitive to thermal neutrons and incorporating seven cylindrical high-density polyethylene (HDPE) moderators that can be added in Russian doll fashion (see Figure 2–11(b)). The cylindrical shape of the NNS moderators allow for an easy fabrication process and quick measurement times. Each moderator is designed to mimic the response function of an equivalent Bonner sphere moderator with thickness ranging from 3 to 10 inches[10]. Once measurements have been made, an unfolding algorithm is applied to obtain a 52-bin spectrum of neutron energies.

He-3 and He-4 Detectors

The detectors used with the NNS are He-3 and He-4 gas-filled detectors (see Figure 2–11(a)). They are contained in a metallic shell and have an active diameter and length of 15.5 mm and 23.8 mm, respectively. They are operated at a voltage of 800 V in pulse-mode and 150 V in current-mode. The He-3 detector is pressurized to 2 atm with the addition of 0.7 atm of krypton as a quench gas. This increases the stopping power of the gas resulting in a greater energy deposition by the reaction products. When thermal neutrons interact with the He-3 gas, a proton recoil reaction (^{3}He(n,p)^{3}H) occurs with a Q-value of 764 keV leading to a peak in the pulse height spectrum at this value (see Figure 2–12). There is, however, presence of a wall effect resulting from nuclear reactions that occur close to walls of the detector. Reaction products produced in this region may not deposit all their energy in the gas because of interaction with the wall. This leads to a low energy tail in the pulse height spectrum.

An important consideration for performing neutron measurements is the presence of photon background. While the He-3 detector is sensitive mainly to neutrons, it can still respond to photons. Thus, a He-4 detector, which is uniquely sensitive to photons and has the same photon response as the He-3 detector, is used to measure the background. The photon signal can then be easily subtracted from the total He-3 response.

Moderators

As mentioned above, the moderators are cylindrically-shaped HDPE shells that are added around the gas-filled detector. In order of increasing diameter, the shells are

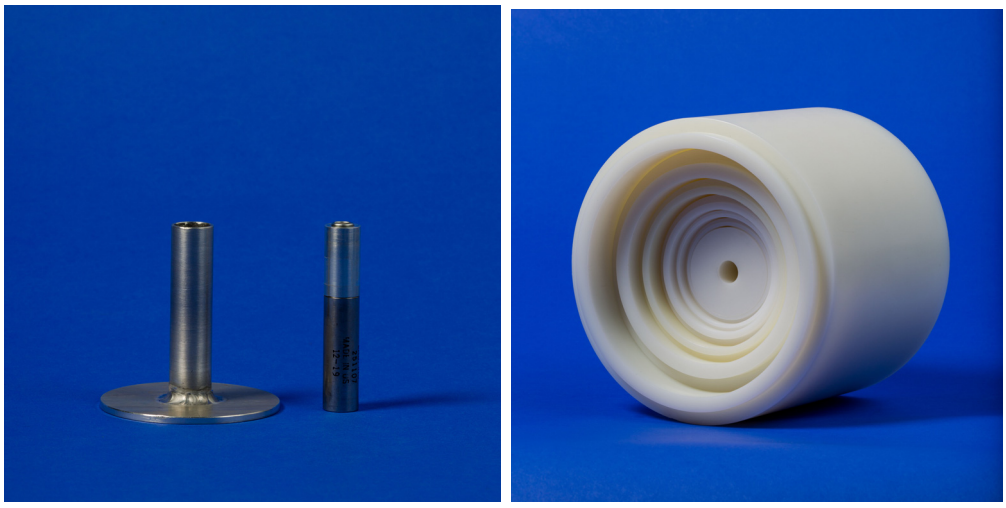

(a) He-3 detector next to its stand for use without moderators.

(b) Largest High-Density Polyethylene moderator with end-caps removed. The detectors are positioned at the center of the cylinders.

Figure 2–11: The Nested Neutron Spectrometer

3, 3.5, 4, 5, 6, 8 and 10 inches wide (see Figure 2–11(b)). Each additional shell is added around the previous smaller combination of shells and sealed with a cap (see Figure 2–13). To transmit the signal from the detector to the electronics, a small hole for a triaxial cable is drilled in the center of each cap.

Response functions for each moderator are determined from Monte Carlo simulations of isotropic radiation incident on the NNS. These were provided by the vendor with units of cm^2 to obtain a fluence rate spectrum after unfolding (see Figure 2–14).

Operation

The NNS can be operated in two modes: pulse and current-mode. In pulse-mode, the signal is amplified by a pre-amplifier and supplied to a multi-channel analyzer(MCA)

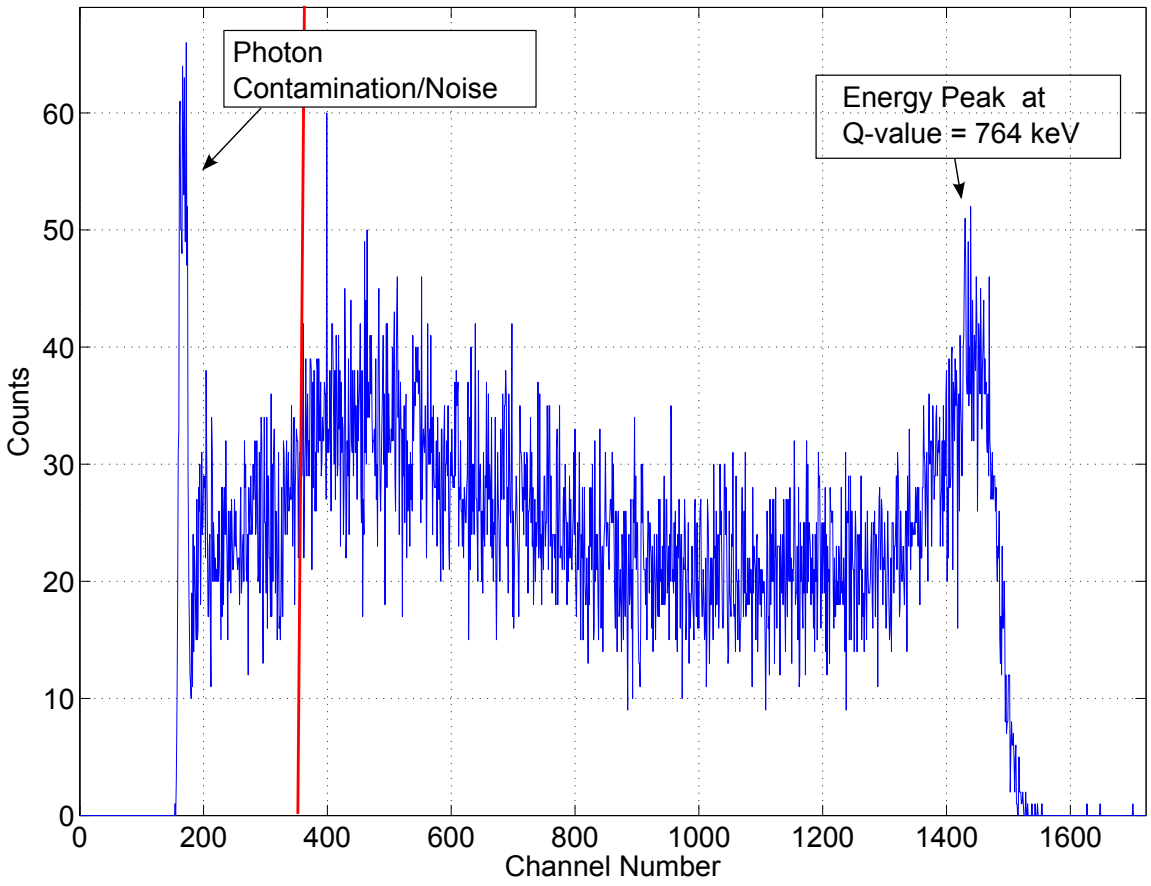

Figure 2–12: Pulse height spectrum of He-3 with the largest moderator irradiated with an AmBe neutron source. The initial cutoff (red) is taken at 200 keV (channel 380).

Figure 2–13: NNS with largest moderator removed and remaining moderator shells.

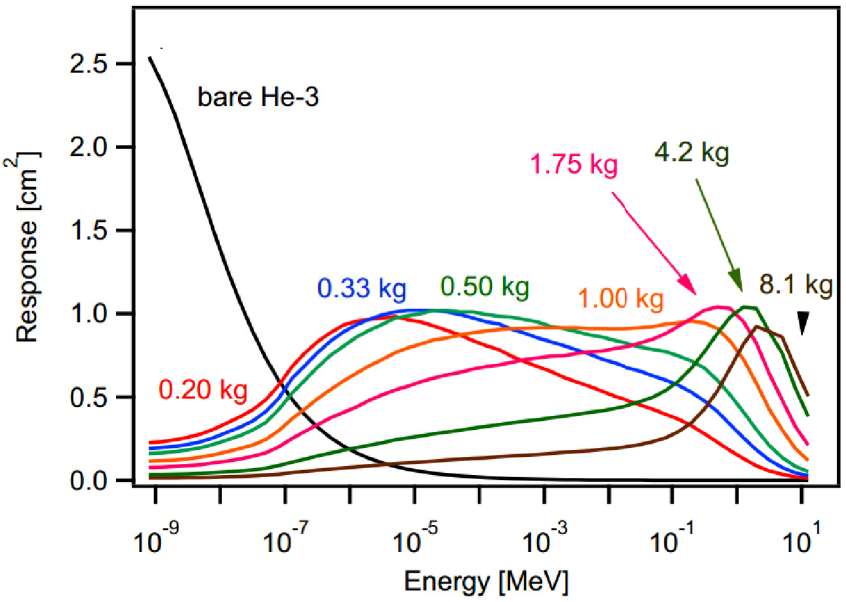

Figure 2–14: Response curves for the NNS. Each moderator is indicated by its mass.

connected to a laptop for viewing the He-3 and He-4 spectra. Neutron counts are selected as those which have an energy greater than 200 keV in the measured spectrum. The counts are then divided by a neutron inclusion factor of 0.82 that accounts for the neutrons that have been neglected using the 200 keV cutoff.

As the moderator is changed, the intensity of the full energy peak changes allowing a deconvolution process to generate a neutron spectrum. However, in many neutron fields a photon background is present. To discriminate neutrons from photons, a He-4 detector sensitive only to photons, may be used in place of the He-3 detector to measure the photon background. Since the photon response of the He-4 detector is similar to that of He-3 but is insensitive to neutrons, the photon signal can be easily subtracted away resulting in a neutron-only signal.

Operated in current-mode, the NNS can measure neutron spectra in high dose rate environments. First, a charge is collected using an electrometer with an applied voltage of +150 V, and converted to an effective current by the time of measurement. Next, the current is converted to an equivalent count-rate so that it may be used directly in the unfolding process. The conversion is easily accomplished by a calibration coefficient, 7 fA/cps, provided by the vendor for the NNS unit used in this study.

Experimental Setup

The NNS is deployed by fixing the sensitive volume of the He-3 or He-4 detector to a point in space. For example, after removal of the largest shell, the remaining shells must be raised by the thickness of the 10 inch shell ($\sim$3 cm). This is achieved using

Figure 2–15: NNS with largest moderator and custom tripod used for measurement.

a custom tripod with appropriately drilled ticks or a custom aluminium stage (see Figures 2–15 and 2–16).

2.5.5 Unfolding

With a set of eight measurements (bare plus seven moderators), it is difficult to generate a spectrum with good energy resolution. This under-determined mathematical problem can be described in the following manner: let m_j be the measurement of the j-th moderator, $A_j(E)$, the response function of the j-th moderator as a function of energy and $n_j(E)$ the neutron spectrum to be found. Then m_j is related to $n_j(E)$

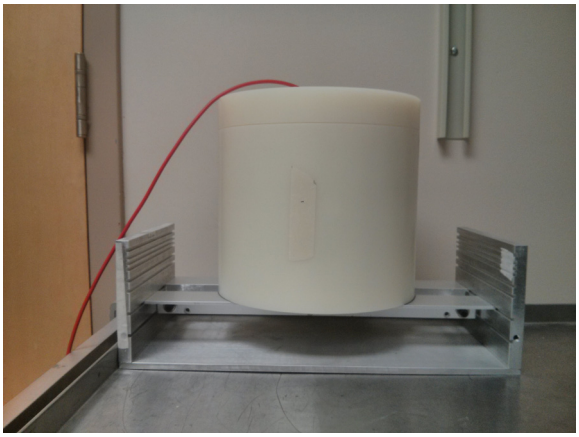

Figure 2–16: NNS with largest moderator and custom stage used for measurement.

by a Fredholm integral of the first kind:

$$m_j = \int_E^{E+\Delta E} A_j(E) n_j(E) dE \tag{2.3}$$

Eq. 2.3 cannot be solved if the response function is unknown as in the case of the NNS. However, $A_j(E)$ can be approximated by a response matrix having discrete values and Eq. 2.3 becomes

$$m_j = \sum_i^N A_{ij} n_j \quad j = 1, 2, \ldots, 8 \tag{2.4}$$

In matrix form, Eq. 2.4 becomes

$$\mathbf{m} = \mathbf{An} \tag{2.5}$$

The simplest solution would be by direct inverse. However, since the matrix is non-square[6] this is not possible. As a result, many methods have been developed to solve this problem including least squares[18], maximum entropy[19] and neural networks[20][21].

With the NNS, a least squares unfolding algorithm, STAY'SL[18], is supplied with proprietary vendor software. While SATY'SL has been used for many years, the software provided was not intuitive, relying heavily on the user and his ability to create meaningful guess spectra. Therefore, in this work, a maximum-likelihood expectation-maximisation (MLEM) [22], which requires minimal knowledge of the measured spectrum, was developed by the author (see Chapter 4).

MLEM is a standard statistical reconstruction tool that is commonly used in positron emission tomography (PET). When applied to convergence, the MLEM algorithm maximises the likelihood of obtaining measured data **m** given that the spectrum is **n**.

Derivation. Let the unknown neutron spectrum be a random vector **n** with mutually-independent Poisson-distributed random variables n_j. Given a response matrix for all moderators with components a_{ij}, the Poisson-distributed measured count-rate m_i can be written as $m_i = \sum_j^n a_{ij} n_j$ with a mean $\bar{g}_i = \sum_j^n a_{ij} \bar{n}_j$. Thus we can write:

$$P(m_i|\bar{g}_i) = \frac{\bar{g}_i{}^{m_i} e^{-\bar{g}_i}}{m_i!} \tag{2.6}$$

[6] Non-square matrices do not have an inverse

The likelihood is the multiplication of all the probabilities for each moderator if the spectrum had been n, or

$$L(\mathbf{n}) = \prod_{i=1}^{n} \frac{\bar{g}_i{}^{m_i} e^{-\bar{g}_i}}{m_i!} \tag{2.7}$$

Taking the logarithm of L and further simplifying we end up with the well known iterative MLEM algorithm:

$$n_j^{k+1} = \frac{n_j^k}{\sum_{i=1}^{N} a_{ij}} \sum_{i=1}^{N} a_{ij} \frac{m_i}{\sum_{b=1}^{J} a_{ib} n_b^k} \tag{2.8}$$

Here, n_b^k is the starting spectrum, n_j^k is the current spectrum estimate, a_{ij} is the response function of the detector and m_i is the measurement in cps. MLEM is a fairly straightforward algorithm and can be described as follows:

1. Create a guess spectrum n_b^1.
2. Convolve this spectrum with the detector response function.
3. Divide the measurement by the result and deconvolve.
4. Update the current estimate of the neutron spectrum.

Evidently, the MLEM algorithm makes use of *a priori* input spectra. These input spectra can have a biasing effect on the end result of the unfolding algorithm and should thus be used with care.

2.6 Monte Carlo Simulations in Health Physics

In radiation protection, particle scatter is the main contributor to dose at any location outside the primary beam. Room shielding design (eg. for the maze or outside the door), may be accomplished using either of two empirical methods: Kersey's method[23] or McGinley's method[24]. These methods are based on generalized

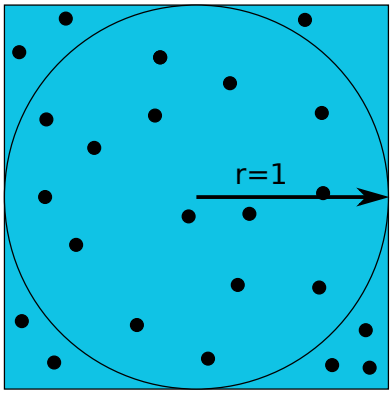

Figure 2–17: Monte Carlo calculation of π. The ratio of areas of the square and the circle is $\pi/4$. In a random sampling of points N inside the square, the fraction falling inside the circle, N_c/N, will converge to the ratio of areas. Thus $\pi = 4N_c/N$.

models and contain many assumptions which can yield uncertainties on the order of 30 %. There is thus a need for more accurate shielding design methods such as the Monte Carlo technique.

The Monte Carlo method was first applied to radiation transport in the 1940s for the development of atomic weapons. Thirty years later, Monte Carlo methods made their first appearance for applications in medical and health physics. However their widespread use was uncommon until the mid 90s due to the lack of computational power. Monte Carlo techniques are now actively used in medical and health physics practice.

2.6.1 Overview of the Monte Carlo Method

The Monte Carlo method is defined as the use of random sampling to determine a statistically expected solution to a problem[25]. It is primarily used for complex problems which cannot be solved using deterministic methods such as the calculation

of π (see Figure 2–17). In radiation transport problems, Monte Carlo methods simulate particles and their interactions with matter as they travel through user-defined geometries. To determine the outcome of each particle interaction, probability distributions are randomly sampled from transport data until the end of that particle's life[7] . Ultimately, the average over many particle interactions is calculated to determine a user-defined score. According to the Central Limit Theorem, as the number of simulated particles increases, the average value will converge to the true value.

2.6.2 Monte Carlo N-Particle Software Version 6.1

The Monte Carlo N-Particle (MCNP) software package version 6.1[8] was developed and is maintained at Los Alamos National Laboratory (LANL). Primarily a photon-neutron transport code, it can also be used for electron, proton and various other particle transport problems. Its applications include, as per MCNP website (`https://mcnp.lanl.gov/`), radiation protection and dosimetry, radiation shielding, radiography, medical physics, nuclear criticality safety, detector design and analysis and many others.

2.6.3 Monte Carlo Parameters in MCNP

As with most Monte Carlo simulation packages, many input parameters define a simulation including geometries, cross sections, source specifications, variance reduction techniques and tallies (quantities of interest).

---

[7] A particle dies if: it reaches zero energy, exits the geometry or is killed/removed by variance reduction techniques

[8] Version 6.1 is a merger between MCNP5 v1.6 and MCNPX.

Geometry and Cross Sections

For radiation transport, the first step in any Monte Carlo technique is defining the geometry of the problem. In MCNP, the geometry is defined through mathematical equations describing surfaces. These surfaces can be combined to create volumes which are termed cells. Once the cell is constructed, it is assigned a material composition and density.

Material compositions are defined by a combination of material specific identifiers, ZAIDs. The Z signifies the atomic number, A, the mass number and ID, the specific library identifier. These identifiers link to specific cross-section data tables which are then weighted to desired material compositions.

Source Specification

MCNP allows the user to define a source in a wide variety of situations as points, surfaces or volumes. Every source is defined by a set of parameters including energy, time, position, and direction. Depending on the choice of these parameters, the computation time can increase significantly.

Tallies, Uncertainty and Variance Reduction Techniques

Tallies in MCNP provide a statistical summary of many particles and can be of three main types: particle current across a surface, particle flux in a volume or energy deposition in a region of interest. They determine an average value over space, energy and time for a given region.

In this project, a tally known as the next-event estimator (F5 tally) simulates neutron fluence at a point. It doubles as a variance reduction method that greatly reduces computation time. When a particle undergoes an interaction, this tally

calculates the probability that the 'next step' directly scatters towards the tally location thus contributing to the average value.

In MCNP, tallies are normalized per starting particle and have an associated relative error E. The relative error is the ratio of the standard deviation of the mean to the mean value of the tally. In any Monte Carlo technique, the relative error can be decreased by increasing the particle histories N. As a rule, the error decreases as $1/\sqrt{N}$. Thus, to decrease the error by a factor of two, the number of histories are multiplied by four.

As the number of histories increases indefinitely, the computation time, T, also increases. In addition, a measure of the efficiency of the calculation is defined as the figure of merit, $FOM = 1/(E^2T)$. Since $E \propto 1/\sqrt{N}$ and $N \propto T$, this implies that $E\sqrt{T} \propto 1$ and is constant. Thus, as the error decreases the computation time must increase. To attain a smaller relative error in a lower computation time, many techniques have been developed to reduce the variance of a tally. These are appropriately termed variance reduction techniques or VRTs. Traditional techniques include low/high energy cutoffs, Russian roulette and splitting[26].

CHAPTER 3
Monte Carlo Modeling of Neutrons in Radiotherapy

Prior to measuring neutron spectra using the NNS, it was important to have some knowledge of the characteristics of the spectrum being measured. Through Monte Carlo simulations, it is possible to create a fully-described model of a linear accelerator and bunker geometry simulating the production of neutrons and scatter. This can be used to compare with and evaluate the final spectrum resulting from neutron measurements with the NNS.

This chapter provides a brief overview of Monte Carlo simulations of photoneutrons in radiotherapy as well as a summary of the particular simulations carried out in this study.

3.1 Status of Photoneutron Modeling in Radiotherapy

Monte Carlo simulations in radiotherapy accurately predict dose distributions in both clinical and research settings. In a review by Verhaegen and Seuntjens [27], Monte Carlo modeling of external beam radiotherapy is described as a process in which the geometry of a linear accelerator and source components are reproduced to simulate clinically relevant treatment beams (see Figure 3–1). Since these beams are mainly composed of photons and electrons, hadrons (neutrons, protons, alpha particles, etc.) are rarely modeled. In radiation safety, these exotic particles, notably neutrons, are of major consideration.

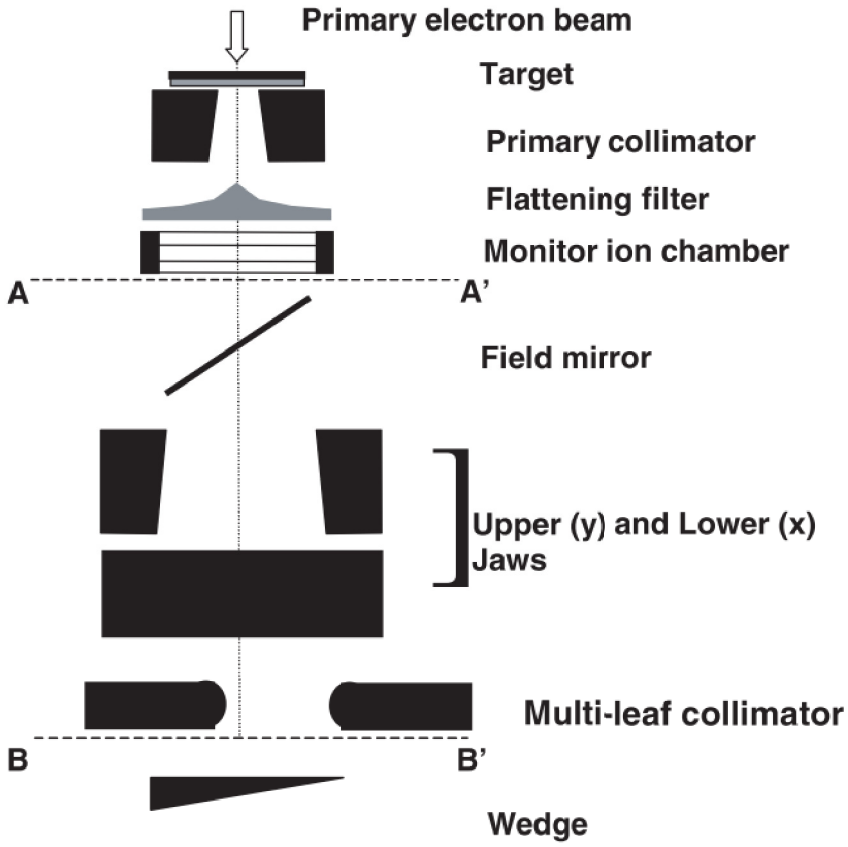

Figure 3–1: Figure showing the main components of a simulated linear accelerator used in medical physics to calculate patient dose. Figure reproduced from *Verhaegen and Seuntjens* [27]

Neutrons in radiotherapy are quantified using a common methodology that consists of comparing a MC model of a linear accelerator (detailed or simplified) and bunker to measured data. In various studies by *Kry et al* [28, 29, 30], *Barquero et al* [31]and *Kase et al* [32], linear accelerator and bunker geometries were modeled to varying degrees of detail. The simulations were compared with measurements using passive neutron detectors such as gold activation foils and thermo-luminescent

detectors. Although, these studies showed good overall agreement between measurements and simulations in some cases differences were up to 30%. This can be attributed to oversimplified accelerator geometry[31] and large detector uncertainties [29, 28, 30, 31, 32].

Accuracy is an important part of any Monte Carlo simulation. A study by *Pena et al*[33] describes the sensitivity of a Monte Carlo simulation to different linear accelerator head and treatment room geometries. They have shown that a fully detailed linac model increases the fluence at isocenter by 80 % compared to a simplified model. This level of sensitivity shows the importance of including all accelerator components in a model and establishing the need to perform sanity checks and validation to account for any inconsistencies.

3.2 Modeling a Varian Clinac 21EX and Bunker Geometry

In this study, a Varian Clinac 21EX (named 21EX-A) located at the Montreal General Hospital was modeled using the published geometry of a Varian 2300C as a template[32]. The beam shaping components and the outer shielding were updated using data from the Varian Monte Carlo Data Package (Varian Medical Systems private communication) and physical measurements of the Varian 21EX undertaken as part of this project. The resulting model of the Varian 21EX is shown in Figure 3–2. It includes the main accelerator components (target, primary collimator, flattening filter, jaws and multi-leaf collimator) along with secondary components (bending magnet, waveguide and bulk shielding).

The bunker was modeled from Montreal General Hospital blueprints of an actual Varian Clinac 21EX bunker (see Figure 3–3). The primary barrier consists of high

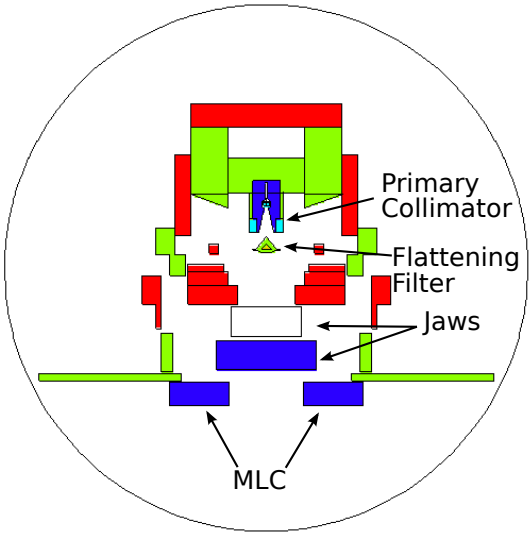

(a) XZ plane. X along the vertical axis and Z along the horizontal axis.

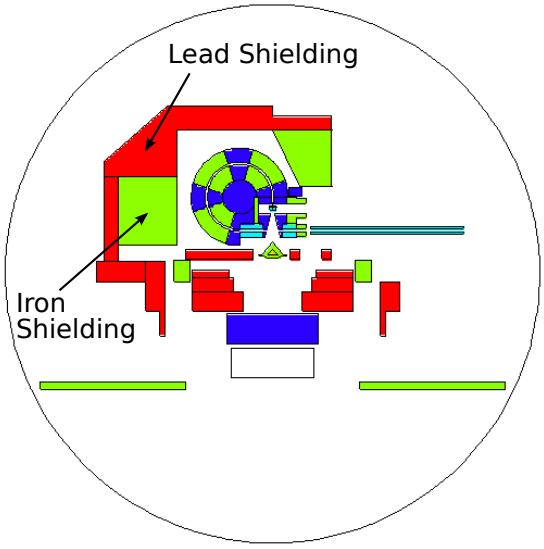

(b) YZ plane. Y along the vertical axis and Z along the horizontal axis.

Figure 3–2: Updated Kase Model of a Varian 21EX. Red is lead, green is iron and blue is tungsten (white signifies that the plane is directly at the interface between two materials). There is a 1:1 scale along the x, y and z axes.

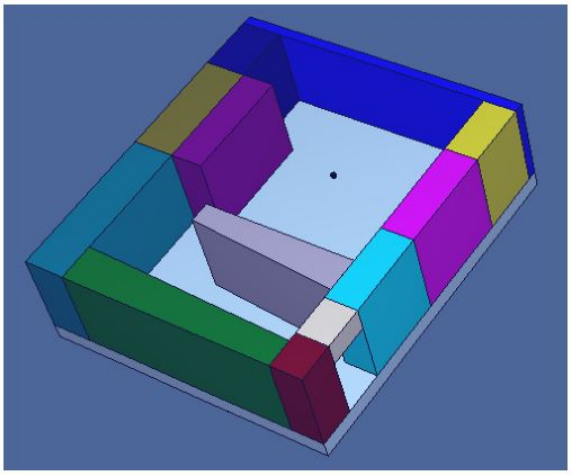

Figure 3–3: Layout of the treatment room for the Varian 21EX-A at the Montreal General Hospital. Colours designate the different sections defined in the simulation. The point at the center of the room is the central position of the accelerator [34].

density concrete (3.53 g/cm^3) while the secondary barriers are all traditional concrete (2.35 g/cm^3).

3.3 Parameter Selection

To simulate neutrons, a set of parameters was defined to model the linear accelerator and bunker: the material cross sections for neutron and photoneutron interactions were taken from the ENDF60 and LA150U data tables, respectively, while the source was defined as a circular region with 18.8 MeV electrons incident on a tungsten target embedded in copper. The energy of electrons was selected after tuning the simulated depth-dose curve to match ion chamber measurements (see Section 3.5). Furthermore, a point-detector tally (F5 in MCNP6) was positioned at various locations (40 cm and 140 cm from the isocenter, at the maze-room junction and in the maze) to simulate fluence at a point. These settings defined the bulk of the simulation.

To speed up simulations, a number of VRTs were used in the model. Each cell (volume) that made up the simulation was assigned equal importance for electrons, photons and neutrons. Although this did not explicitly speed up the simulation, equal importance (used in splitting/Russian roulette to eliminate particles) ensured that no particles were terminated or duplicated by Russian Roulette [26]. Furthermore, a maximum energy cutoff was set to 20 MeV. This allowed all high energy particles to be transported since the energy of starting electrons was 18.8 MeV. Next, a low energy cutoff of 6.5 MeV killed any particle below the set value. This cutoff was chosen based on the photonuclear threshold energies of the linac materials as shown in Table 2–1.

3.4 Sensitivity Analysis

A sensitivity analysis can help determine the level of dependence on the model through a series of tests. In this work, the effect of the walls, the furring and the accelerator shielding materials were studied. The following figures are plots of neutron spectra with units of neutrons per squared cm per starting electron[1] . In each of the following tests, simulations were run on a cluster of 32 CPUs of varying speeds. Typical simulation time was 2-3 hours with 1 billion starting electrons.

3.4.1 Barrier Effect

The effect of the walls on the neutron spectrum at 140 cm from the isocenter was investigated by successively extending the walls and then removing them altogether

[1] MCNP normalizes the F5 tally to the number of initial particles, in this case electrons

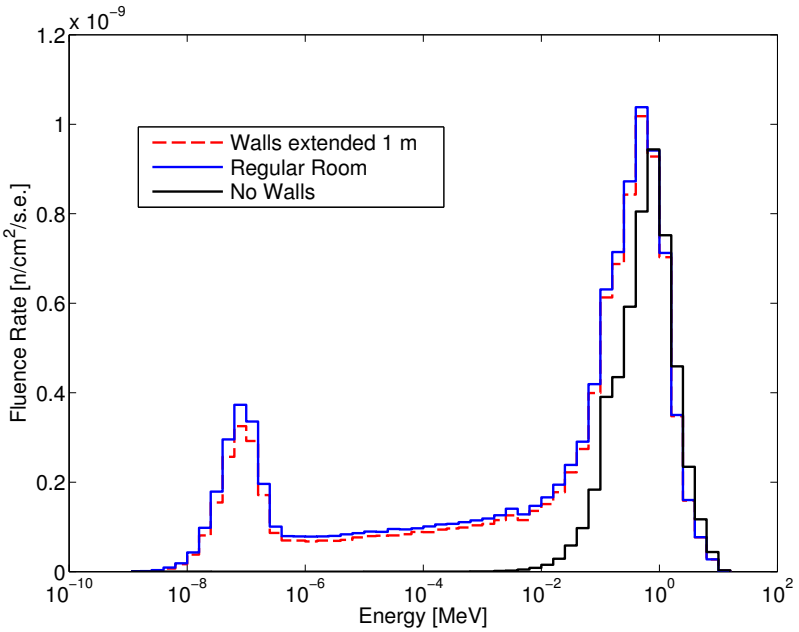

Figure 3–4: Effect of extending and removing the room walls on the neutron spectrum. As the wall are extended outward, the thermal peak decreases to zero.

(see Figure 3–4). By extending the walls by one meter, the thermal peak decreased slightly. This showed that the room does not have a significant effect on the neutron spectrum. However, as a sanity check, the walls were also completely removed. As expected, the thermal peak and intermediate energies were completely absent. The lack of neutron scatter with the room walls prevented high energy neutrons from losing their energy resulting in the absence of thermal and intermediate energies.

3.4.2 Furring Effect

The effect of adding 8 cm of wood (cellulose) paneling to the walls was also studied. The additional material on the walls served to mimic storage, cabinets and many other objects inside a real radiotherapy treatment room. Wood, with its large hydrogen content, added another layer of moderation for neutrons scattering off the

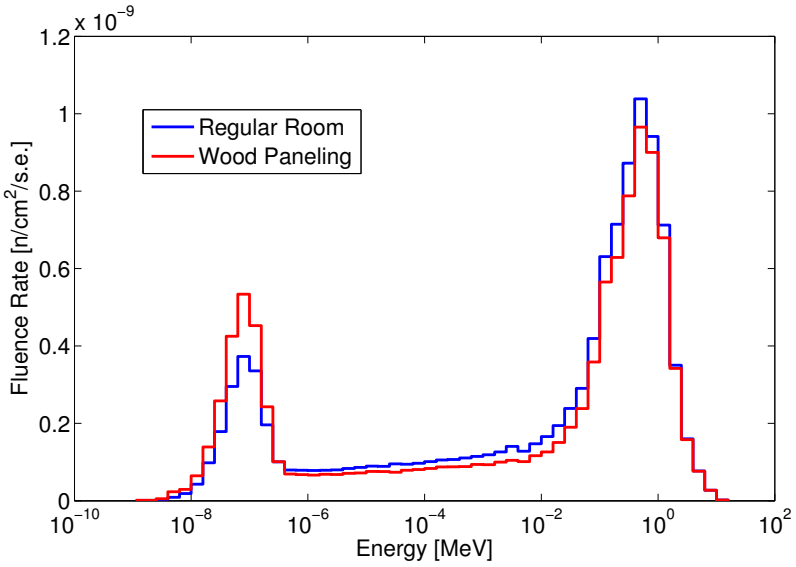

Figure 3–5: Effect of overlaying wood (cellulose) paneling on the walls to mimic furnishing. The thermal peak is increased by 30%.

walls. As expected, an increase in the thermal neutron peak of approximately 30% compared with the regular room was observed at 140 cm from the linac head as shown in Figure 3–5.

3.4.3 Accelerator Shielding Effect

Different materials within the linac head have different photonuclear cross sections and interaction probabilities. Changing the material of the shielding in the linac head will therefore have an impact on the neutron spectrum surrounding the linac. To study this, the shielding material around a simplified linac head [2] was changed from lead to iron to tungsten; the main materials found in an accelerator. In Figure

[2] The shielding components in Figure 3–2 were removed and replaced with a cylinder for simplicity.

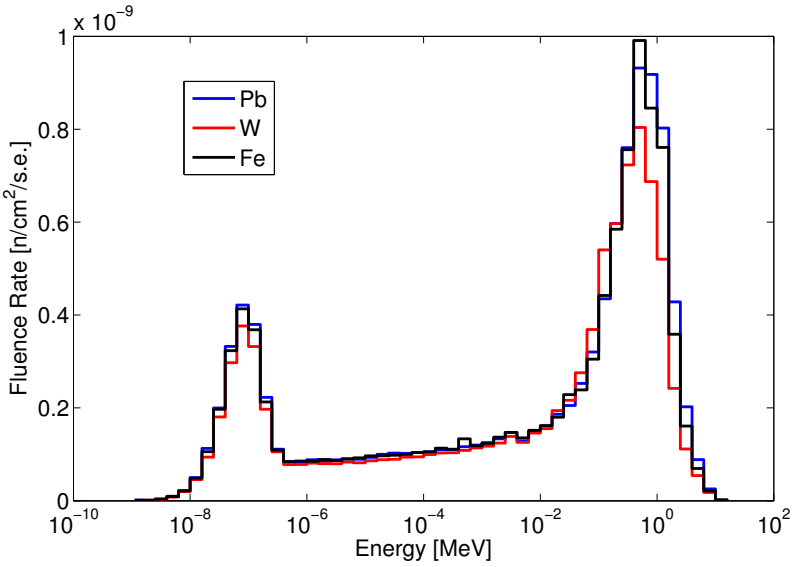

Figure 3–6: Effect of changing the shielding material on a simplified linac. Tungsten shielding decreased the fast neutron peak by 20% compared to iron or lead.

3–6, the effect of the different materials is shown. There was little difference between lead and iron. However, tungsten shielding decreased the fast neutron fluence by approximately 20 % compared to the iron or lead. This can be attributed to the greater density and larger total neutron cross section of the tungsten which inevitably increases the attenuation of neutrons.

Throughout these tests, the characteristic shape of the spectrum remained fairly constant. The only changing feature observed through sensitivity tests was a change in fast neutron peak intensity. Thus, the MC model reproduces the general spectral characteristics for a neutron spectrum in radiotherapy[14] in a consistent way.

3.5 Reference Simulation

One of the goals of this project was to build a Monte Carlo model that could accurately predict the neutron spectra in a radiotherapy bunker. This model was used

to evaluate the feasibility of using a Nested Neutron Spectrometer in high dose-rate environments by comparing the characteristics of the measured and simulated spectra. However, in absolute terms, spectra could not be directly compared because of a difference in units. MCNP outputs units of n/cm^2 per starting electron, whereas NNS measurements (see Section 2.5.4) yield n/cm^2/s. As such, a calibration method was developed to compare simulated and measured spectra.

Spectra were compared using two different methods: the normalization method and calibration method. In the first method, an arbitrary value (the maximum) was chosen as the normalization point in each spectrum. This removes units from both simulation and measurement and provides a quick and easy way to compare spectra. However, this method creates a bias to the point of normalization. Given the shape of the spectra in the previous section, normalizing to the fast neutron peak would force agreement at that peak and create a discrepancy at the other. If the normalization is taken at the thermal peak, the opposite situation occurs as shown in Figure 3–7. For this reason, another method that preserves the realistic shape of the spectra was devised.

The second method was to obtain an absolute comparison of simulated and measured data by calibrating the MC simulation. The general approach to this method is shown in Figure 3–8. The idea was to relate the neutron fluence per starting electron to a neutron fluence per Gy of photon dose in reference conditions. A measurement in reference conditions at the Montreal General Hospital are defined as: 10×10 cm^2 field, 100 cm source to surface distance (SSD) and 100 cGy at the

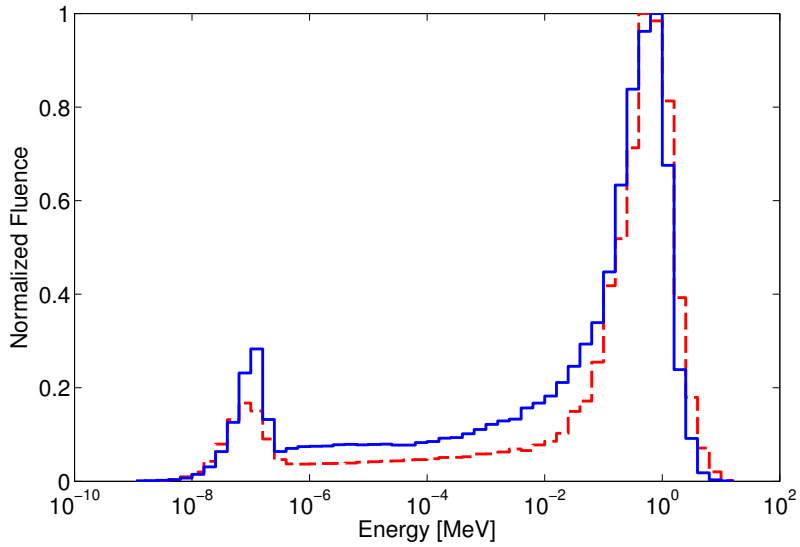

(a) Spectrum normalized to the maximum of the fast neutron peak

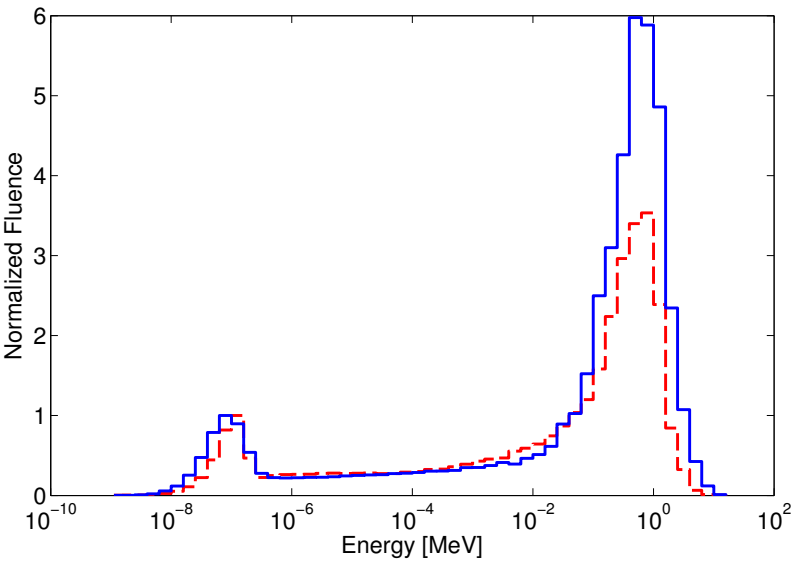

(b) Spectrum normalized to the maximum of the thermal neutron peak

Figure 3–7: Two different normalization schemes. The two figures show the biasing effect of selecting a normalization point at either the fast or thermal neutron peaks.

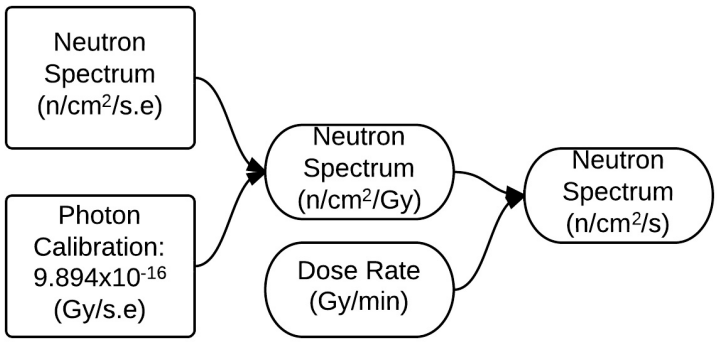

Figure 3–8: Process to convert Monte Carlo fluence spectra to n/cm^2/s. Every value in the neutron spectrum is multiplied by the inverse of the photon calibration to yield units of n/cm^2/Gy. Multiplying by dose rate and adjusting for time, the neutron spectrum can be compared on the same scale as measurements.

depth of maximum dose (D_{max}). In these conditions, the accelerator in calibrated so that 100 cGy produces 100 monitor units (MU) of charge in the monitor chamber.

As mentioned previously, units of the MC simulated data were n/cm^2 per starting electron. To relate this to fluence per Gy of photon dose, a photon calibration simulation was setup in MCNP: a $30 \times 30 \times 30$ cm^3 volume of water with $2 \times 2 \times 1$ cm^3 voxels was placed with its upper surface at 100 cm from the source (target). The energy deposited by electrons in the water was tallied to obtain a photon PDD under reference conditions as per the AAPM TG-51 protocol [35]. Next, the MC model was tuned (by varying the electron energy) to match this PDD with that measured using a MicroLion ionization chamber as shown in Figure 3–9. All of the measurement points are within the 2% error bars of the simulated depth dose curve. This allowed the photon model to be benchmarked against measurements.

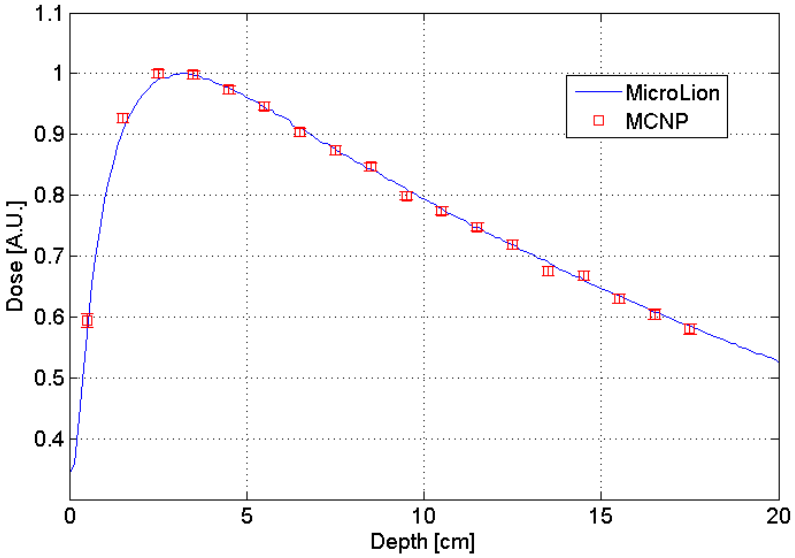

Figure 3–9: Percent depth dose curves of a Varian 21EX linac simulated using MCNP and measured using a clinical ionization chamber for reference conditions.

With a tuned photon model, a calibration coefficient for the neutron fluence, 9.894×10^{-16} n/cm^2/s.e, was obtained from the depth of maximum dose D_{max} of the simulated photon PDD. Since the simulations were defined using the TG-51 protocol, the value at D_{max} is equal to the reference condition of 100 cGy/100 MU. This value, in Gy per starting electron, was used to convert neutron fluence *per starting electron* in the simulated spectra to a neutron fluence *per Gy of photon dose* at the depth of maximum dose. With knowledge of the dose rate, the value was then converted to neutron fluence per second. Using this method, it was possible to directly compare, in an absolute manner, simulations and measurements of photoneutron spectra in a radiotherapy bunker (see Chapter 4).

CHAPTER 4
Feasibility of Measuring Neutron Spectra in Radiotherapy Facilities with a NNS

This chapter describes the evaluation of the NNS in four steps: (1) validation of a custom-developed MLEM algorithm to reproduce neutron spectra, (2) performance tests around a linac, (3) comparison of NNS-measured equivalent dose with bubble detector measurements and (4) comparison of NNS-measured neutron spectra with those generated by Monte Carlo simulations.

4.1 A New MLEM Algorithm

In Chapter 2, the theory of the MLEM algorithm was discussed in relation to neutron spectrum unfolding. Here the parameters for operation of the algorithm are discussed in detail.

The MLEM algorithm was coded by the author in MATLAB given its ability to perform matrix operations. It takes five parameters as input: a set of eight measurements, an initial guess spectrum, a response matrix (see Section 2.5.4), a stopping criterion and a cutoff.

4.1.1 Measurement Data

The measurement data is input to the MLEM function as a set of eight measurements in counts per second. This is required by the response functions to obtain a fluence-rate over 52 bins ranging from thermal to fast energies.

4.1.2 Input Spectra

Selecting an initial spectrum is critical to avoid bias in the final spectrum. Ideally, the true spectrum will be somewhat known prior to unfolding so an initial guess can be made. This is true in the case of reference spectra where the NNS is calibrated and tested. However, in radiotherapy, the characteristic spectrum around a linear accelerator is not well known.

Initially, an unbiased uniform spectrum was selected to be the initial guess spectrum for unfolding radiotherapy neutron spectra. This was tested by convolving MC neutron spectra with the response functions of the moderators and subsequently unfolding them with the MLEM algorithm. When comparing the original and unfolded MC spectra there was a systematic underestimation of thermal neutrons. As a result, a step function was tested and selected as the best initial guess to increase the amount of thermal neutrons (see Figure 4–1).

4.2 Stopping Criterion and Cutoff

The MLEM algorithm always converges. However, if no stopping criterion is applied, it will run indefinitely or start to acquire noise. In this study, we have set a stopping criterion which stops the algorithm when the difference between the measured data and the convolved spectrum, $m_i - \sum_j^n a_{ij} n_j$, reaches a minimum value. In the event that noise overtakes the algorithm as a result of poor data, a hard cutoff is set at 10000 iterations of the algorithm[1] .

[1] A typical numbers of iterations is $\sim$5000

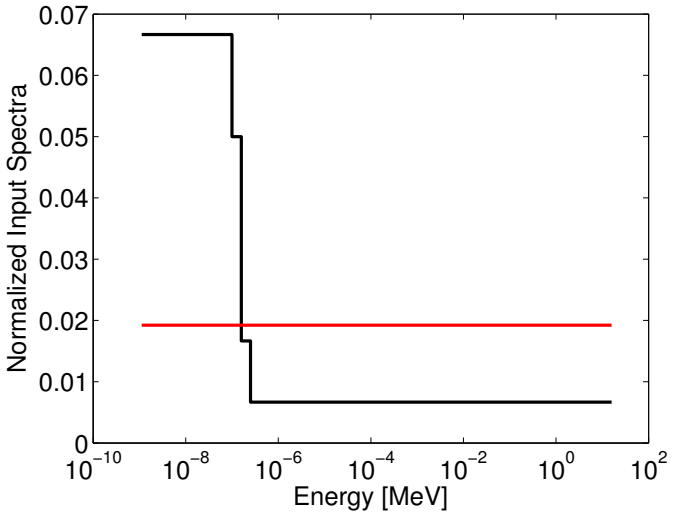

(a) Input spectra used for unfolding. Red is the uniform input, black is the selected step function.

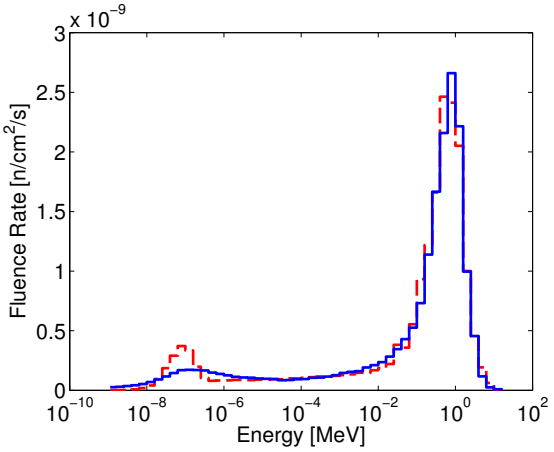

(b) Comparison of original MC (red) and unfolded MC (blue) using a uniform input function.

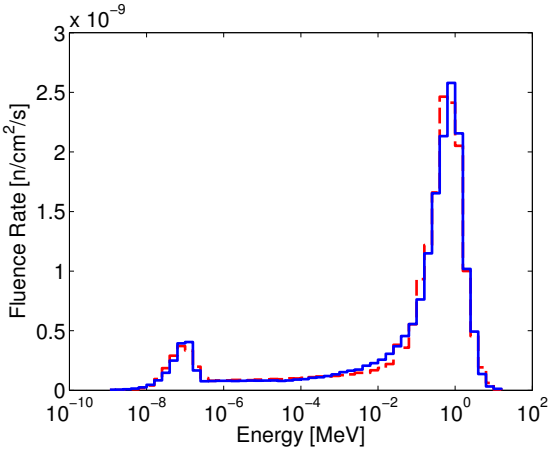

(c) Comparison of original MC (red) and unfolded MC (blue) using a step input function.

Figure 4–1: Input spectra and outcome of final spectrum after unfolding with MLEM.

4.3 Validation of the MLEM Algorithm for Spectrum Unfolding

A He-3 detector is only sensitive to thermal neutrons. To obtain an energy spectrum that spans the range of neutron energies in radiotherapy (thermal to fast neutrons), response functions[2] for each moderator are used to deconvolve measured data. This can be done using various unfolding algorithms, as described in Section 2.5.5.

In this study, we developed a maximum likelihood expectation maximization algorithm (see Section 2.5.5) to iteratively unfold neutron spectra. To validate the algorithm, a series of tests needed to be performed. These tests involved comparing MLEM-unfolded spectra to either reference spectra or spectra reproduced by other unfolding algorithms.

4.3.1 Reference Neutron Spectra

Reference neutron spectra such as Cf-252, AmBe or PuBe are generally used for calibration (see Table 4–1 for details). These sources provide a stable neutron fluence that can be used to validate response functions and newly-developed algorithms by comparing measurements with published reference spectra. In this work, data provided by the manufacturer of the NSS from an unmoderated Cf-252 source, a D2O moderated Cf-252 source[3] and an AmBe source (see Section 4.3.4) were used for validation of our MLEM algorithm. Neutrons produced by the source were detected

[2] A response function describes the sensitivity of the detector and moderator over a range of neutron energies.

[3] All data was graciously provided by Detec. Measurements were carried out by Detec at NIST.

Table 4–1: Characteristics of various neutron sources used in calibration of neutron detectors. Table adapted from ISO-8529-1 standard[36]. S_{av} is the spectrum averaged fluence-to-dose equivalent conversion coefficient and Ψ is the fluence-average energy.

Source	Half-life (years)	Ψ (MeV)	S_{av} (pSv·cm^2)
D_2O Moderated Cf-252	2.65	0.55	105
Cf-252	2.65	2.13	385
AmBe (α, n)	432	4.1	391

using the NNS by the manufacturer, reconstructed using MLEM and compared to the published reference. A good agreement between reconstructed and reference spectra served as validation.

4.3.2 Cf-252

MLEM-reconstructed and reference data for the unmoderated Cf-252 are shown in Figure 4–2. At first glance, the two spectra agree very well in the fast energy region. Upon further inspection, there is a noticeable peak in the thermal energy region for the measured data. This is expected because of the scatter in the facility at the National Institute of Standards and Technology (NIST); a result of some neutrons scattering off the walls and air and interacting with the detector.

4.3.3 Moderated Cf-252

Unlike bare Cf-252, moderated Cf-252 produces thermal to fast neutrons. This allows us to verify the sensitivity of the algorithm over a larger energy range. In this case, reference data were measured by Detec at NIST using the NNS and unfolded using their proprietary least squares algorithm [18]. The same data was also unfolded using

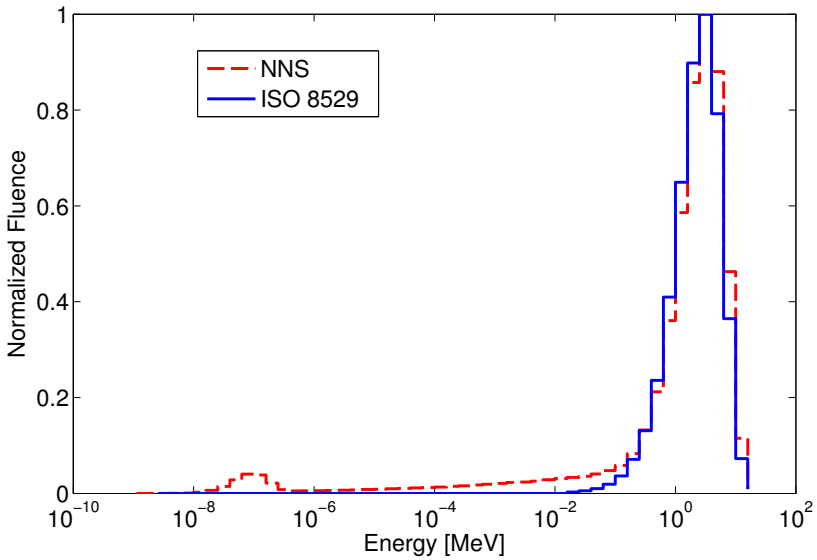

Figure 4–2: Comparison of the ISO 8529 bare Cf-252 reference spectrum with NNS-measured data. A good agreement is observed in the fast neutron peak. A thermal neutron peak is present for the NNS-measured data due to room scatter.

our MLEM algorithm[4] . There is very good agreement between the MLEM and least squares algorithms as shown in Figure 4–3. However, there are local differences up to 5% between the two algorithms.

Since the spectra for the moderated Cf-252 are un-normalized, it is also possible to compare the total fluence-rate. The total fluence rate is a measure of how well the algorithm preserves the total neutron counts in the unfolding process. Although this should not differ significantly in either case, there are some uncertainties (response functions, small number of initial measurements, etc) in each algorithm that may

[4] Input spectra were the same in both cases.

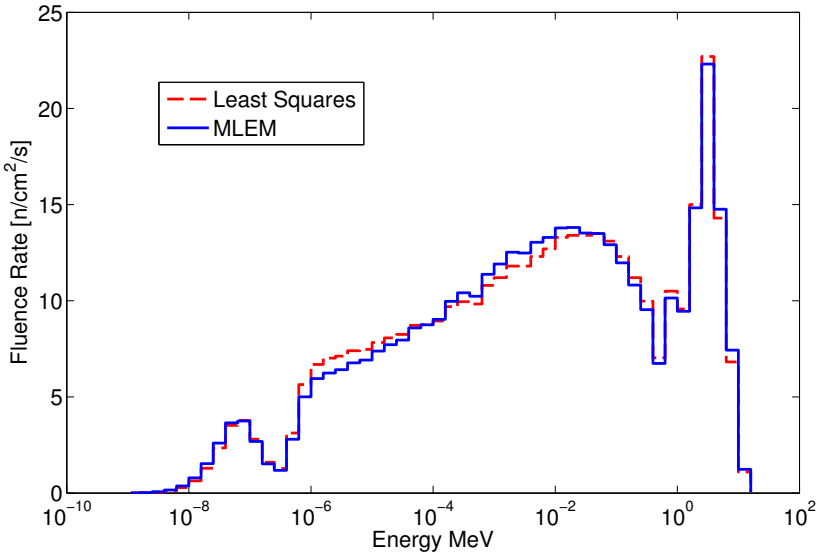

Figure 4–3: Comparison of NNS measured data of a D2O moderated Cf-252 neutron source. The neutron spectra were reconstructed using two different algorithms: least squares (Detec) and MLEM (This work).

introduce errors. Nevertheless, comparing MLEM and least squares algorithms, the total fluence is 399.9 n/cm^2/s and 400.1 n/cm^2/s respectively; a difference of 0.05 %.

4.3.4 Comparison Using an AmBe Source at NRC

The neutron spectrum of an AmBe source encapsulated in steel (12.6 n cm^{-2} s^{-1} at 1 m, $T_{1/2}$ = 470 years) was measured by our group at the neutron laboratory of the National Research Council Canada (NRC). The objective was to validate the MLEM algorithm while measuring the neutron spectra of an AmBe source with the NNS operated in pulse-mode.

In pulse-mode, the He-3 detector was positioned 20 cm away from the AmBe neutron source (see Figure 4–4). It was connected to a preamplifier followed by

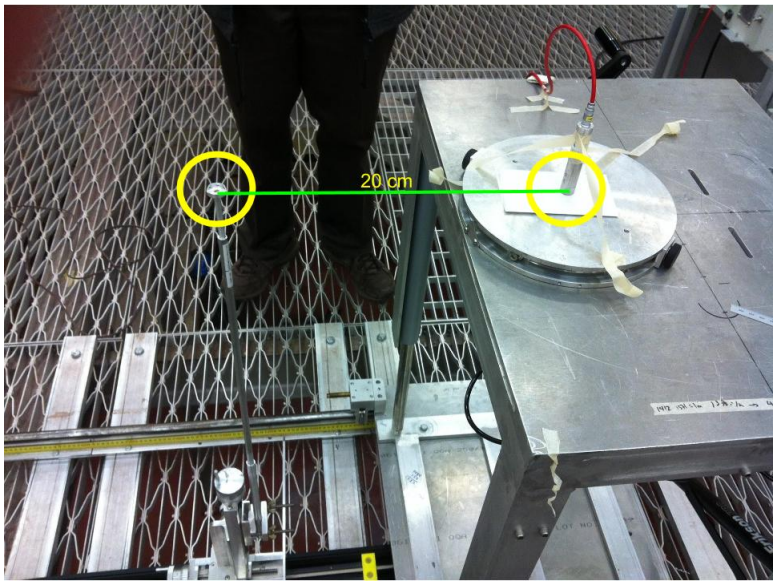

Figure 4–4: Setup of experiment with source at 20 cm from the detector.

Table 4–2: Raw data as measured in pulse-height. The counts are obtained from the pulse-height spectrum above 200 keV to remove gamma and electronic noise.

Moderator	**He-3 [Counts/min]**
7	13322
6	13365
5	10718
4	7823
3	3883
2	2941
1	1712
0	16

an URSA II multi channel analyzer (MCA) (S.E. International INC., Summertown, USA). The MCA was connected to a computer where a custom program by Detec Inc displayed the pulse-height spectrum for each moderator similar to Figure 2–12. The count-rate was determined from the number of counts above 75 keV to remove electronic noise and gammas, the results of which are shown in Table 4–2. As expected, there is a clear decrease from large to small moderator; at high energies, the largest moderators yielded the greatest response while the bare detector yielded the lowest. However, between moderators six and seven, there is a similar response. This occurs because of the similarity of the response functions for moderators six and seven.

Finally, the neutron spectra were reconstructed using the MLEM algorithm and compared to an AmBe reference spectrum. This is shown in Figure 4–5. There was good agreement between the NNS-measured and ISO reference spectra. However, at low energies there is a clear systematic difference between the measured and reference spectra. This is due to room and air scatter of the facility at NRC.

These results, combined with those of the bare and moderated Cf-252, serve as a validation of the MLEM algorithm.

4.4 The Nested Neutron Spectrometer in Radiotherapy

Radiotherapy linear accelerators deliver radiation in very short pulses, a few milliseconds apart. This translates to high dose-rates that can paralyze many detectors. Detector paralysis comes from the inability of the electronics to distinguish individual events.

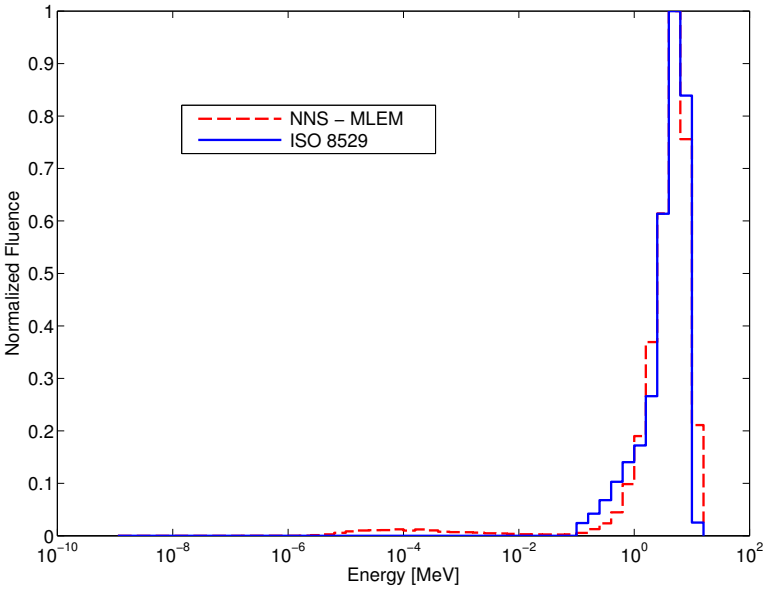

Figure 4–5: Comparison between NNS measured spectrum and ISO reference spectrum of an AmBe neutron source.

With the NNS, pulse-mode is suitable at count rates up to 10 000 counts per second. In a radiotherapy treatment room, count-rates can reach up to 1 000 000 counts per second, dismissing the possibility of operating the NNS in pulse-height.

Current-mode, on the other hand, does not exhibit detector paralysis. The first use of a current-mode in high dose rate environments using a Bonner sphere system was established by Hagiwara [37]. In the same manner, current-mode was used in this project to perform neutron spectroscopy around a medical linear accelerator. In the next sections, the NNS in current-mode is evaluated for radiotherapy environments.

4.4.1 Experimental setup

All validation measurements made use of the Varian Cinac 21EX-A linear accelerator at the Montreal General Hospital. This linac is capable of producing high energy

photons (up to 18 MV) and electrons (up to 20 MeV). In addition, the 21EX-A can deliver radiation at dose rates up to 600 MU/min (600 cGy/min).

In this work, linac settings were the following: 18 MV photons at a dose rate of 600 MU/min and gantry positioned at 0°. The jaws were closed to limit the photon leakage as much as possible and to increase photoneutron production.

As for detector positioning, the NNS could have been positioned at any location in the treatment room. However, to obtain high dose rates, the NNS was placed on the treatment couch with the center of its sensitive volume 40 cm away from the isocenter on the couch (see Figure 4–9). Without being directly in the primary beam, the detector was nevertheless immersed in a high neutron field. It is always positioned in the upright position with the tri-axial cable coming out of the top of the moderator as in Figure 2–16.

4.4.2 Reproducibility, Linearity and Dose Rate

To evaluate the use of the NNS in radiotherapy three tests were carried out to examine its performance: reproducibility, linearity and dose rate.

Reproducibility. The reproducibility of NNS measurements was evaluated using the setup described in the previous section. At 40 cm from the isocenter, neutron measurements were repeated three times. The mean count rate, standard deviation and coefficient of variation (standard deviation divided by the mean) for each moderator are shown in Table 4–3. The COVs are larger than expected for statistical fluctuations up to a factor of five for the mid to large moderators. This can be due to the high gamma incidence on the detector and noise in the system. However,

Table 4–3: Mean count rate, standard deviation and relative error for each of the seven moderators plus bare detector. Conversion to count-rate was performed using the manufacturer calibration coefficient 7 fA/cps.

Moderator	He-3 Mean (CPS)	He-3 Stdv (CPS)	COV (%)
7	306094	1996	0.65
6	553198	2375	0.43
5	791706	3845	0.49
4	805786	3551	0.44
3	696540	1101	0.16
2	591968	1790	0.30
1	455579	601	0.13
0	91611	202	0.22

since COVs did not exceed 0.65 %, this demonstrated that NNS measurements are reproducible around a linac.

Even though the measurements are reproducible, this does not imply that the unfolded neutron spectrum will necessarily remain the same. Indeed, the unfolded neutron spectra generated from the data in Table 4–3 and shown in Figure 4–6 are not identical. The differences between unfolded spectra show that even though the reproducibility is very good, the unfolding process is sensitive to small changes.

Linearity. As is the case for reproducibility, the dose rate should remain stable as the total irradiation time increases. For this test, the total MU delivered was increased by 600 MU three times: the first measurement was 600 MU, the second was 1200 MU and the third was 1800 MU. To evaluate linearity, the ratio of count rates for each irradiation are plotted with respect to moderator number in Figure 4–7. As expected, the ratios remained relatively unchanged to within 0.5%.

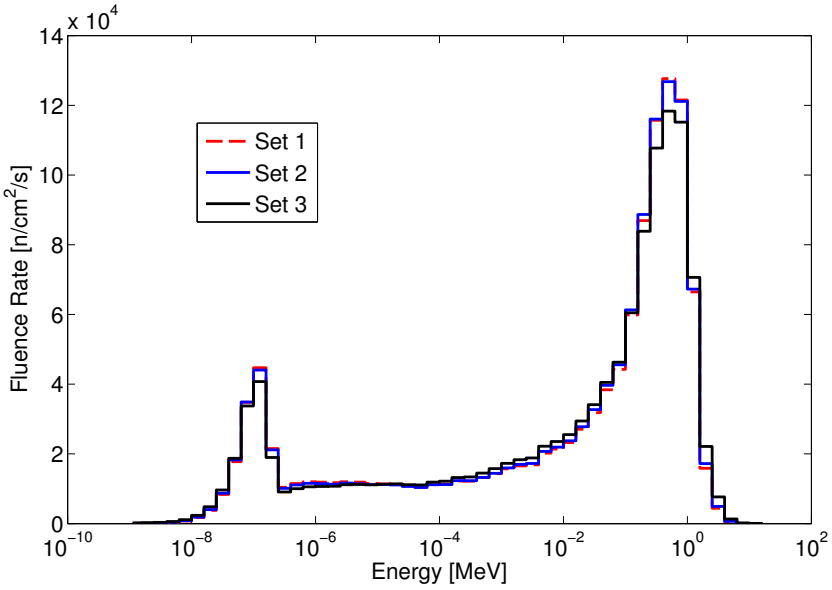

Figure 4–6: Comparison between three measurements in identical setup.

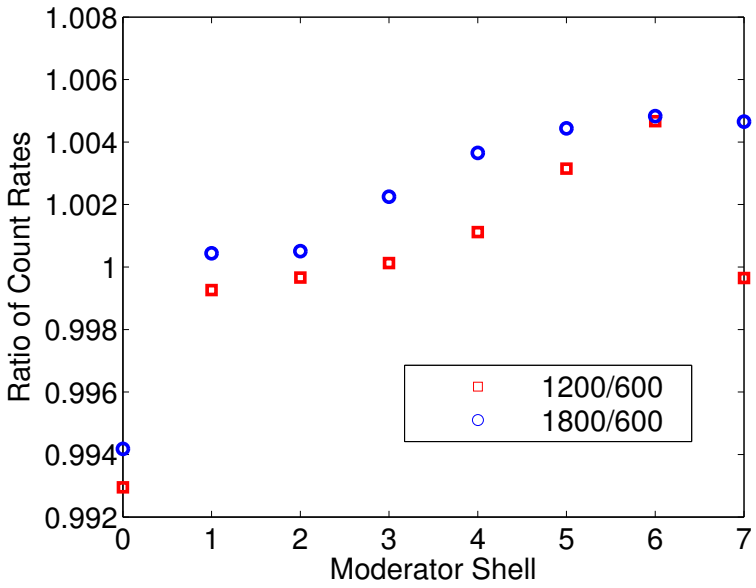

Figure 4–7: Ratio of count rates for 1800/600 and 1200/600.

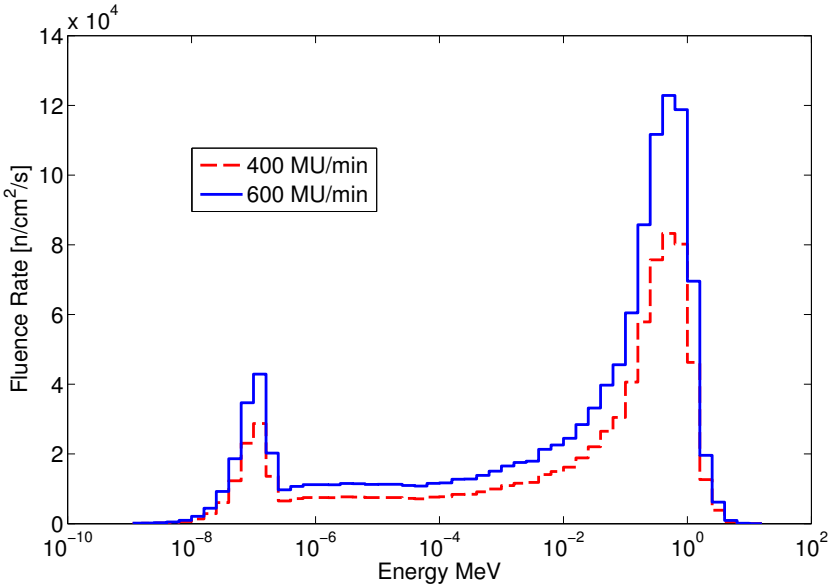

Figure 4–8: Comparison between 400 MU/min and 600 MU/min. The ratio of the total fluence is 0.67.

Dose Rate. Unlike reproducibility and linearity, decreasing the photon dose rate of the linac was expected to reduce the count rate of each moderator by the ratio of dose rates. In this experiment, the photon dose rate was changed from 600 MU/min to 400 MU/min; a ratio of 0.67. This resulted in total fluence rates of 1.21×10^6 n/cm^2 and 0.81×10^6 n/cm^2 for 600 MU/min and 400 MU/min respectively. The ratio of the two fluences yielded 0.67; exactly as expected.

Ultimately, reproducibility, linearity and dose rate tests demonstrated that the high dose rates in radiotherapy do not adversely affect the performance of the NNS operated in current-mode.

Directional Response. A directional response was carried out by the manufacturer in the presence of an AmBe source. Two directions were evaluated: the detector upright (perpendicular to the source) and with its axis directly facing the

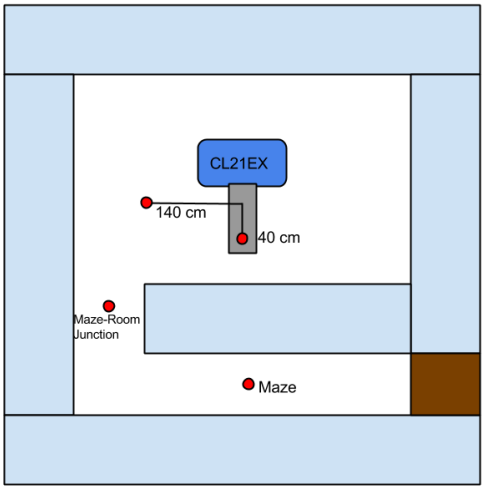

Figure 4–9: Bubble detector and NNS measurement locations inside the bunker of the Varian CL21EX at the Montreal General Hospital. The location at 40 cm was used only for NNS reproducibility tests.

source. There was an observed difference up to $\sim 10\%$ between the two detector directions with the upright direction exhibiting the greater response[11]. As it stands we have not performed a directional response study around the linear accelerators and requires further investigation.

4.4.3 Comparison with Bubble Detectors

One of the most effective methods for validating a new detector is by comparing it to another well established detector. In this research project, bubble detectors (see Section 2.5.3) were used to measure independently the equivalent dose at various points in the treatment room as shown in Figure 4–9.

Two bubble detectors, PND and BDT (BTI Technology Industries, Chalk River, Canada) were used at each location. The PND detector is sensitive to intermediate

Table 4–4: Summary of bubble detector measurements in a Varian 21EX-A treatment room at the Montreal General Hospital.

(a) Number of MU at each point of measurement. The MU in the maze were increased to 340 because of the low number of fast neutrons arriving at the point of measurement.

	140 cm	M-R Junction	Maze
BDT (MU)	5	20	60
PND (MU)	5	20	340

(b) Equivalent dose-rates measured by NNS and bubble detectors. ICRP-74 fluence-to-dose conversion coefficients are used to convert the NNS spectral fluence rates to dose.

	140 cm	M-R Junction	Maze
NNS (mSv/hr)	383.0	56.7	1.1
PND+BDT (mSV/hr)	390 ± 40	62 ± 9	2.2 ± 0.7
Difference (%)	**1.25**	**8.45**	**50**

and fast neutrons ($E_k > 200$ keV) while the BDT detector is sensitive to thermal and epithermal neutrons. Using these two bubble detectors positioned upright on a tripod at the height of the isocentre, a total equivalent dose corresponding to the spectrum in radiotherapy was determined by summing the two measurements. For each measurement, the total MU was adjusted to account for position in the treatment room so as to provide better counting statistics (see Table 4–4(a)): in the maze, the neutron fluence rate was much lower than in the treatment room. Therefore, to obtain better counting statistics, the number of MU was increased.

Bubble detectors are radiation dosimeters that are calibrated to measure personal equivalent dose[5] . To compare with the NNS, the NNS-measured spectra were multiplied by fluence-to-equivalent dose conversion coefficients taken from ICRP-74 [38]. The results are shown in Table 4–4(b). Dose differences as measured by the NNS and bubble detectors varied from 1 % in the room to 50 % in the maze. Near the linac, $\sim$100 bubbles were produced in the detector resulting in good counting statistics, while the total number of bubbles produced in the maze was just $\sim 10-15$. This translated to a Poisson uncertainty for the measurements in the maze of approximately 60 % at 2σ, which means that the NNS and bubble detector measurements agreed with each other within their uncertainties. Apart from the uncertainty in the maze results, the NNS accurately reproduced the equivalent doses in the treatment room that were measured by bubble detectors.

4.4.4 Comparison with Simulations

Using the same positional set-up as the bubble detector experiment, neutron production was simulated using MCNP and measured using the NNS at various points in the bunker of the 21EX-A.

The simulated and NNS-measured spectra are shown in Figures 4–10 and 4–11. Close to the linac head, at both 40 cm and 140 cm from the isocenter, the spectra agree well. There is, however, a discrepancy in the the fast neutron peak between

[5] Personal equivalent dose is defined as the dose equivalent in soft tissue, at an appropriate depth, d, below a specified point on the body

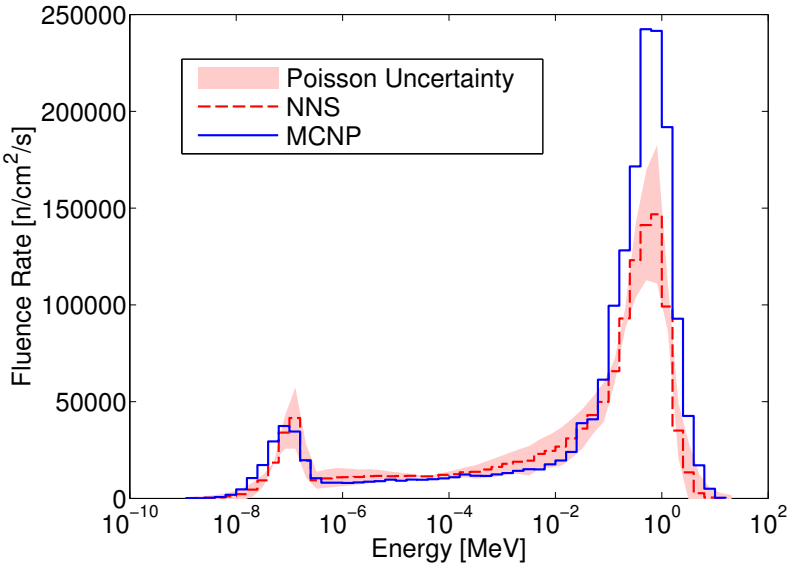

(a) Neutron spectrum at 40 cm from the isocenter on the patient plane. Both MCNP-simulated and NNS-measured spectra are shown.

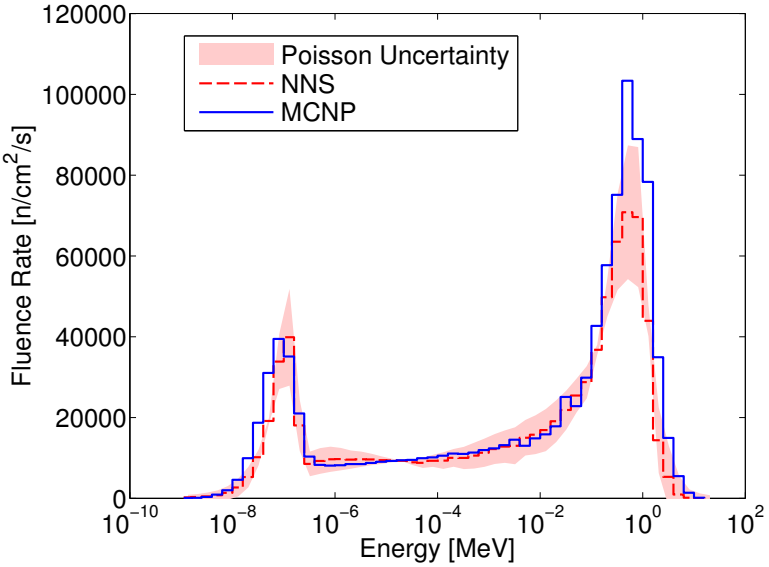

(b) Neutron spectrum at 140 cm from the isocenter. Both MCNP-simulated and NNS-measured spectra are shown.

Figure 4–10: Neutron Spectra at locations closest to the head of the Varian 21EX.

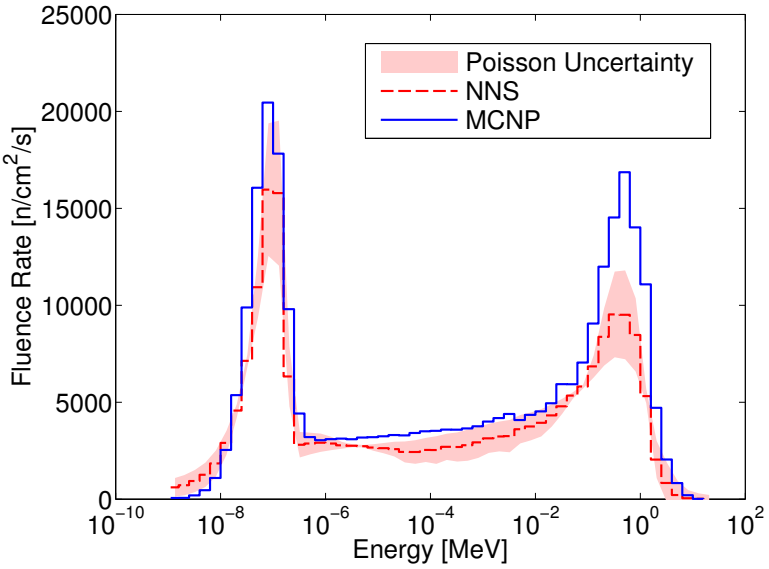

(a) Neutron spectrum at the maze-room junction. Both MCNP-simulated and NNS-measured spectra are shown.

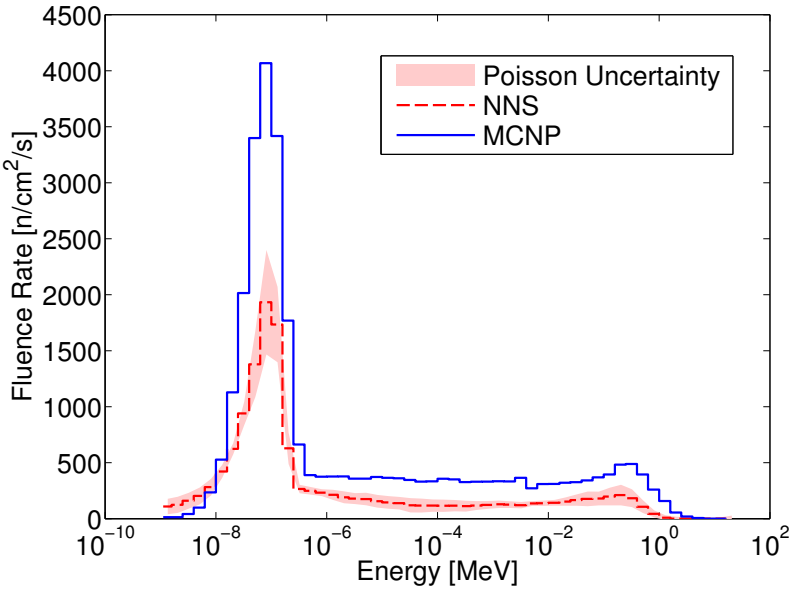

(b) Neutron spectrum in the bunker maze. Both MCNP-simulated and NNS-measured spectra are shown.

Figure 4–11: Neutron spectra at the farthest point from the Varian 21EX.

the simulations and measurements. The FWHM and the mean energy of the fast peaks are in agreement although their intensities are not.

For the previous measurements of equivalent dose, the NNS results agreed very well with the bubble detectors in the room. However, a closer inspection of the fluence to dose calculation reveals that a number of different combinations of neutron spectra can potentially yield the same equivalent dose. Also, there are many uncertainties associated with the measurements: Poisson uncertainty, unfolding uncertainty, response function uncertainty and input spectrum uncertainty. Only the Poisson uncertainty is shown in the figures, however the combination of the other uncertainties may easily account for the observed discrepancy in the peak heights.

Another possible cause of the discrepancy is that the model of the 21EX-A was not exact; much of the shielding is based on the Varian 2300 linac which may not accurately represent the 21EX-A. Even though the photon component (see Section 3.5) agreed very well with the ionization chamber data and the statistical uncertainty for each of the spectral bins were less than 5 %, the incomplete data pertaining to the shielding components might contribute to the discrepancy between the neutron measurements and simulations.

As the point of measurement is displaced from inside the room (Figures 4–10(a) and 4–10(b)) toward the maze (Figures 4–11(a) and 4–11(b)), the fast neutron peak is strongly suppressed as expected. The neutrons that reach the maze have undergone a number of scattering interactions with the concrete. Towards the end of the maze, a large fraction of thermal neutrons have been absorbed by the walls and maze door.

This leads to a thermal neutron peak present in the maze 100 times less than that in the room.

In the maze, Figure 4–11(b), there is a large difference in the relative intensity of neutrons between the simulations and NNS spectra. There is approximately a factor of two ion intensity across the spectra. Upon further inspection of the fast neutron peak at 40 cm, the simulation is also approximately 50% larger. The factor of two difference in the fast neutron peak between simulation and measurement would inevitably contribute to the greater overall increase of simulated neutrons obeserved in the maze.

Finally, the characteristic peak locations and magnitudes of the spectrum are important when comparing simulated and measured spectra. For both simulations and NNS spectra, the peak locations and relative intensity between peaks agree well; this demonstrates that the NNS does indeed reproduce a real neutron spectrum.

CHAPTER 5
Effect of Flattening Filter Free Beams on Neutron Spectrum

With the rapidly changing design of modern linear accelerators and treatment techniques, it is becoming important to re-evaluate the production of neutrons in a radiotherapy treatment room. This is particularly true for new accelerators that offer flattening filter free beams and thus an expected reduction in neutron dose. In the previous chapter, the NNS was validated as a useful tool for measuring neutron spectra in radiotherapy. It permits the user to measure neutron spectra quickly and efficiently using an active measuring technique. In this chapter, the validated NNS was used to characterize the neutron spectrum of a new linear accelerator, the Varian TrueBeam, in flattening filter free mode.

5.1 Flattening Filters and Neutron Production

Flattening filters (FF) are high-Z conical-shaped attenuators that are positioned in the beam line of a medical linear accelerator. They compensate for the radial variation in energy and intensity of primary photons and are designed to produce a uniform or flat dose distribution at a certain depth (10 cm) in water. Historically, these flat dose distributions allowed physicists to calculate manually patient doses for treatment planning. When the first computerized treatment planning systems were developed, early calculation algorithms used an interpolation technique that required flat dose profiles. Ever since, flattening filters have been included in the design of medical linear accelerators[39].

Recently, with the advent of sophisticated Monte-Carlo based dose calculation algorithms, there has been an interest in removing the flattening filter for treatment[40, 41, 42]. One advantage of doing this is to increase the dose rate for the same electron current hitting the target. Since flattening filters are composed of thick high-Z materials, they highly attenuate the beam passing through them. Removing the flattening filter thus allows the linac to operate at much higher dose rates decreasing treatment times.

Another possible advantage, which is investigated here, is the expected reduction in photoneutrons produced in the head of the linear accelerator. Removing the flattening filter translates to less material for photons to interact with. Since fewer photons are being attenuated and scattered, per monitor unit, there will are fewer neutrons produced. In *Kry et al.* [29], the authors measured the reduction in neutron fluence near a Varian Clinac 21EX with the flattening filter removed. They observed a reduction of 30% in the neutron ambient dose equivalent per gray of photon dose. Since flattening filters do not change drastically from one accelerator to the next, we expect approximately the same reduction for the TrueBeam as for the Clinac 21EX measured by *Kry et al.*.

5.2 Experimental Setup

The NNS was used to compare the neutron spectrum produced by flattened and un-flattened beams at energies of 10 MV and 10 MV FFF. In each case, the Varian TrueBeam linac at the Jewish General Hospital was positioned with the gantry at 270° so that the target was closest to the maze-room junction. The jaws remained closed throughout the measurements and the dose rate was set to 400 MU/min for one

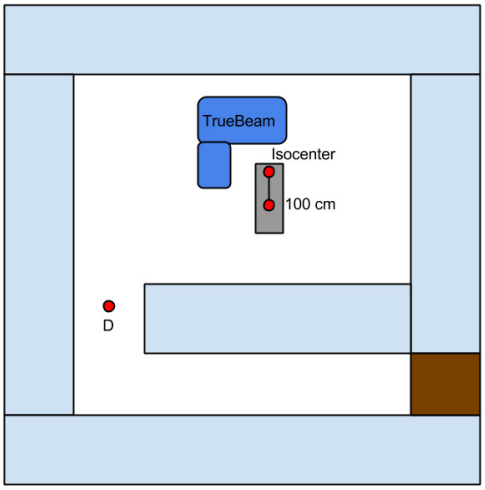

Figure 5–1: Measurement locations inside the bunker of the Varian TrueBeam at the Jewish General Hospital.

minute. Measurements were taken at three locations: one meter from the isocentre and the maze-room junction(see Figure 5–1). Measurements in the maze were too noisy and were thus neglected in the interest of time.

In current mode, the He-3 and He-4 detectors were connected directly to a Keithley electrometer (model no. 6517A) (Keithley, Cleveland, USA) and operated at +150 V. Charge was collected for 60 seconds for each of the seven moderators and the bare detector.

5.3 Neutron Spectra, Fluence and Source Strength

The unfolded spectra for the 10 MV and 10 MV FFF beams at 100 cm from the isocenter and at the maze-room junction are shown in Figures 5–2 and 5–3. There is a notable decrease in neutron fluence in all areas of the spectrum for the 10 MV

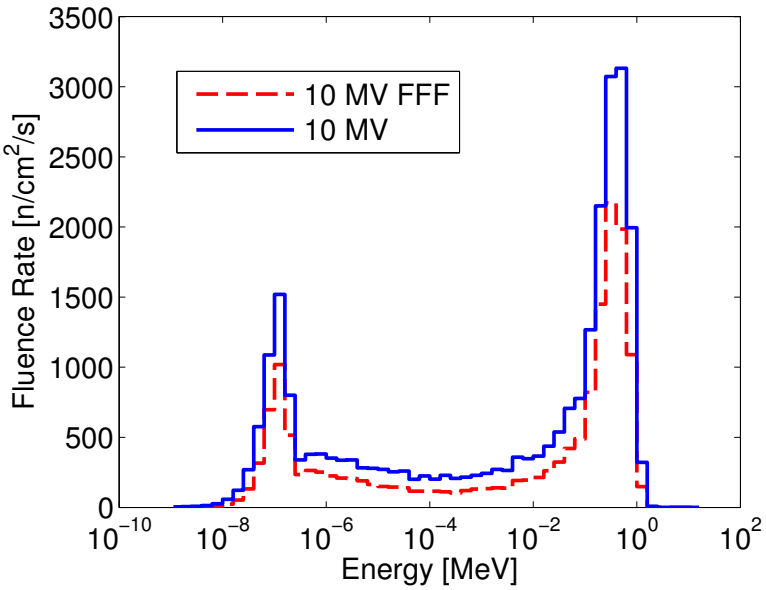

Figure 5–2: Neutron spectrum of the 10 MV and 10 MV FFF modes of the Varian TrueBeam at 100 cm from the isocenter on the patient couch.

FFF beams at both locations. This is due in part to the lower number of photons (emitted at the target) necessary to obtain one monitor unit.

Visually comparing the results of the neutron spectrum produced by the Varian 21EX from the previous chapter and the Varian TrueBeam in this chapter, there is a consistent shape between neutron spectra: a large fast neutron peak and a smaller yet important thermal peak. This suggests that the flattening filter has little effect on the shape of the spectrum. The observed difference in overall neutron intensity results from the reduced electron current (and thus photon fluence exiting the target) necessary to produce 1 MU of radiation. However, the machines are not identical and so this requires further investigation.

The total decrease in neutron production for the flattening filter free mode can be quantified by calculating the total flux of the spectrum (see Table 5–1) which

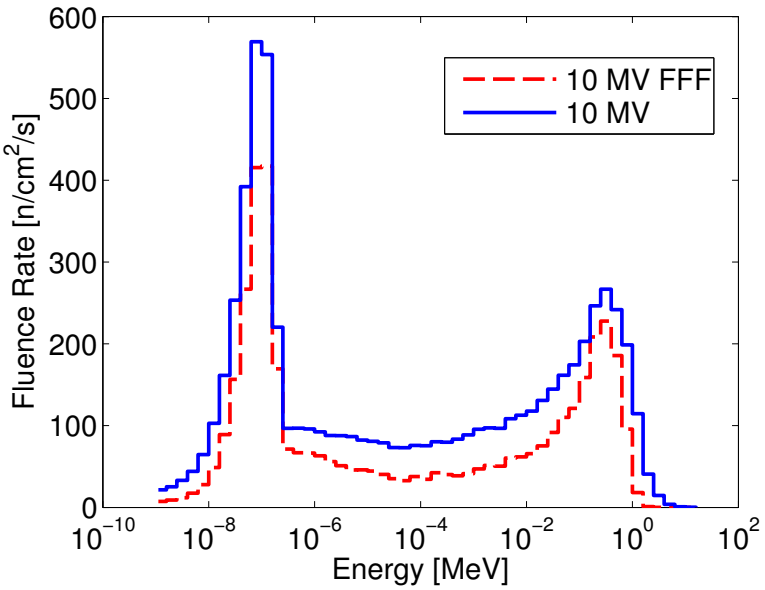

Figure 5–3: Neutron spectrum of the 10 MV and 10 MV FFF modes of the Varian TrueBeam at the maze-room junction.

is equivalent to the area under the neutron spectrum. There is an overall decrease in neutron flux of approximately 40 % between the 10 MV beam and the 10 MV FFF beam. Similarly, by using ICRP-74 fluence-to-dose conversion coefficients [38], the ambient dose equivalent H*(10)[1] was calculated to be, again, about 40 % less. Finally, a quantity useful in radiation shielding, the neutron source strength Q_n which is defined as the neutrons emitted from the accelerator head per gray of x-ray

[1] H*(10) is the dose equivalent that would be produced by the corresponding expanded and aligned field in the ICRU sphere at a depth d, on the radius opposing the direction of the aligned field[43].

Table 5–1: Flux, ambient dose equivalents and neutron source strengths for the 10 MV beam in conventional and FFF mode of the Varian TrueBeam. ICRP 74 fluence to dose conversion coefficients were used to convert fluence to equivalent dose.

Location	Beam Energy	Flux ($\times 10^4 \frac{n}{cm^2 s}$)	H*(10) (mSv/hr)	Q_n ($\times 10^{12}$ n/Gy)
Couch	10 MV	2.57	10.6	0.060
	10 MV FFF	1.59	6.6	0.037
D	10 MV	0.65	1.4	-
	10 MV FFF	0.41	0.8	-

absorbed dose at the isocenter[2] , was calculated from the data at 140 cm from the isocenter to be 0.06×10^{12} n/Gy and 0.037×10^{12} n/Gy for the 10 MV and 10 MV FFF beams, a decrease of 38 %.

Ultimately, these results demonstrate that flattening filter free treatments can be beneficial to both patients and personnel in terms of reduced neutron dose. For the patient, the decreased production of neutrons contributes to a lower whole body neutron dose that will reduce the risk of second cancers. As for personnel, reduced neutron production can lead to less neutron activation in the room. This decreases the amount of residual radiation remaining in the room after a high-energy treatment.

[2] $Q_n = \Phi_{dir+sca+th}\left(\frac{a}{4\pi d^2} + \frac{5.4a}{S} + \frac{1.26}{S}\right)^{-1}$ where Φ is the fluence due to direct, scattered and thermal neutrons, a is the material transmission coefficient, d is the distance from the point of measurement to the target and S is the surface area of the room [43].

CHAPTER 6
Conclusion and Future Work

In this research project, neutron spectra in radiotherapy were studied using a Nested Neutron Spectrometer and a custom developed unfolding algorithm based on maximum likelihood expectation maximization. Firstly, the custom MLEM algorithm was validated by unfolding measured data and comparing these with Cf-252 standard reference spectra. MLEM-unfolded neutron spectra agreed very well with their respective reference spectra.

Secondly, the feasibility of measuring neutron spectra with the NNS in high dose-rate environments was validated around a Varian Clinac 21EX at the Montreal General Hospital. Reproducibility, linearity and dose-rate tests were all evaluated and found to be within 1% for raw data. However, because of the low number of measurements and high number of unfolding bins, it was observed that small changes in the measured data affected the final neutron spectrum. To evaluate the total neutron production, the equivalent dose measured by the NNS was compared to that measured by bubble detectors. These measurements agreed with each other within uncertainty at all measurement locations.

The final validation step was to characterize the shape of the neutron spectrum produced by the NNS. To this end, a Monte Carlo simulated neutron spectrum of a fully described linear accelerator and bunker was compared with that measured by the NNS. There was good overall agreement between measurement and simulation

except for a discrepancy in the peak heights of the fast neutron peak close to the linear accelerator. This translated to an overall increase in the amount of simulated neutrons reaching the maze compared to that measured by the NNS.

All considered, the NNS operated in current mode was deemed a suitable neutron spectrometer for high dose rate environments. As such, the NNS was used to measure the neutron spectrum produced in conventional and FFF mode around the new Varian TrueBeam at the Montreal Jewish General Hospital. At each point of measurement, there was a notable decrease of approximately 40% in the fluence rate and ambient dose equivalent near the linac head as well as the neutron source strength in the treatment room.

6.1 Future Work

While the agreement between Monte Carlo-simulated and NNS-measured neutron spectra was good overall, there were some discrepancies that may be resolved by accurately modeling the geometry of the entire linac and shielding. The Varian 2300C and CL21EX linacs have approximately the same physical dimensions but some shielding components are likely quite different. This is even more apparent in the Varian TrueBeam model; the shielding is completely remodeled to a single piece of tungsten rather than individual lead blocks. With accurate linac models, it should be possible to reliably calculate the neutron spectrum given the bunker geometry. This would potentially provide a basis for patient-specific risk estimates for the development of second cancers from neutrons during radiotherapy.

REFERENCES

[1] Statistics Canada, "Table 102-0561 - Leading Causes of Death, Total Population, by Age Group and Sex, Canada, Annual," CANSIM database Table 102-0561, Ottawa: Statistics Canada, Ottawa, Ontario, July 2012.

[2] Advisory Committee on Cancer Statistics, "Canadian cancer statistics 2013," tech. rep., Canadian Cancer Society, Toronto, ON, 2013.

[3] R. T. Skeel and S. N. Khleif, *Handbook of cancer chemotherapy*. Lippincott Williams & Wilkins, 2011.

[4] J. Kildea, *An evaluation of NCRP report 151–radiation shielding design for radiotherapy facilities, and a feasibility study for 6 MV open-door treatments in an existing high-energy radiation therapy bunker*. PhD thesis, McGill University (Canada), 2010.

[5] E. B. Podgorsak, *Radiation physics for medical physicists*. Springer, 2010.

[6] ICRP, "The 2007 Recommendations of the International Commission on Radiological Protection," tech. rep., ICRP, 2007.

[7] F. Brooks and H. Klein, "Neutron spectrometry—historical review and present status," *Nuclear Instruments and Methods in Physics Research Section A: Accelerators, Spectrometers, Detectors and Associated Equipment*, vol. 476, no. 1, pp. 1–11, 2002.

[8] D. S. Followill, M. S. Stovall, S. F. Kry, and G. S. Ibbott, "Neutron source strength measurements for Varian, Siemens, Elekta, and General Electric linear accelerators," *Journal of applied clinical medical physics / American College of Medical Physics*, vol. 4, pp. 189–94, January 2003.

[9] R. Barquero, R. Méndez, M. Iniguez, H. Vega, and M. Voltchev, "Thermoluminescence measurements of neutron dose around a medical linac," *Radiation protection dosimetry*, vol. 101, no. 1-4, pp. 493–496, 2002.

[10] R. L. Bramblett, R. I. Ewing, and T. Bonner, "A new type of neutron spectrometer," *Nuclear Instruments and Methods*, vol. 9, no. 1, pp. 1–12, 1960.

[11] J. Dubeau, S. S. Hakmana Witharana, J. Atanackovic, a. Yonkeu, and J. P. Archambault, "A neutron spectrometer using nested moderators," *Radiation protection dosimetry*, vol. 150, pp. 217–22, June 2012.

[12] IAEA, "Handbook on photonuclear data for applications," tech. rep., IAEA-TECDOC-Draft No 3, March 2000.

[13] National Committee on Radiation Protection and Measurements (U.S.), *Shielding for High-energy Electron Accelerator Installations: Recommendations of the National Committee on Radiation Protection and Measurements*. No. 13 in NCRP report, U.S. Government Printing Office, 1964.

[14] C. Domingo, M. García-Fusté, E. Morales, K. Amgarou, J. Terrón, J. Roselló, L. Brualla, L. Nuñez, R. Colmenares, F. Gómez, G. Hartmann, F. Sánchez-Doblado, and F. Fernández, "Neutron spectrometry and determination of neutron ambient dose equivalents in different linac radiotherapy rooms," *Radiation Measurements*, vol. 45, no. 10, pp. 1391 – 1397, 2010.

[15] P. Rinard, "Neutron interactions with matter," tech. rep., Los Alamos, 2009.

[16] D. Hamilton, "Neutron interactions with matter," September 2006. 8th Multi-Media Training Course with Nuclides.net.

[17] J. S. E. Townsend, *Electricity in gases*. Clarendon Press, 1915.

[18] F. Perey, "Least-squares dosimetry unfolding: The program STAY'SL," *ORNL/TM-6062*, 1977.

[19] M. Reginatto, P. Goldhagen, and S. Neumann, "Spectrum unfolding, sensitivity analysis and propagation of uncertainties with the maximum entropy deconvolution code MAXED," *Nuclear Instruments and Methods in Physics Research Section A: Accelerators, Spectrometers, Detectors and Associated Equipment*, vol. 476, no. 1, pp. 242–246, 2002.

[20] C. C. Braga and M. S. Dias, "Application of neural networks for unfolding neutron spectra measured by means of Bonner spheres," *Nuclear Instruments and Methods in Physics Research Section A: Accelerators, Spectrometers, Detectors and Associated Equipment*, vol. 476, no. 1, pp. 252–255, 2002.

[21] M. Matzke, "Unfolding procedures," *Radiation protection dosimetry*, vol. 107, no. 1-3, pp. 155–174, 2003.

[22] A. P. Dempster, N. M. Laird, D. B. Rubin, *et al.*, "Maximum likelihood from incomplete data via the EM algorithm," *Journal of the Royal statistical Society*, vol. 39, no. 1, pp. 1–38, 1977.

[23] R. Kersey, "Estimation of neutron and gamma radiation doses in the entrance mazes of SL75-20 linear accelerator treatment rooms," *Medicamundi*, vol. 24, no. 3, pp. 151–155, 1979.

[24] P. H. McGinley, "Photoneutron production in the primary barriers of medical accelerator rooms," *Health physics*, vol. 62, no. 4, pp. 359–362, 1992.

[25] Los Alamos National Laboratory report LA-UR-03-1987, *X-5 Monte Carlo Team, MCNP–A General Monte Carlo N-Particle Transport Code, Version 5 - Vol. I: Overview and Theory*, April 2003.

[26] A. F. Bielajew and D. W. Rogers, "Variance-reduction techniques," in *Monte Carlo Transport of Electrons and Photons*, pp. 407–419, Springer, 1988.

[27] F. Verhaegen and J. Seuntjens, "Monte carlo modeling of external radiotherapy photon beams," *Physics in medicine and biology*, vol. 48, no. 21, p. R107, 2003.

[28] S. F. Kry, U. Titt, F. Ponisch, O. N. Vassiliev, M. Salehpour, M. Gillin, and R. Mohan, "Reduced neutron production through use of a flattening-filter-free accelerator," *International journal of radiation oncology, biology, physics*, vol. 68, pp. 1260–4, July 2007.

[29] S. F. Kry, R. M. Howell, U. Titt, M. Salehpour, R. Mohan, and O. N. Vassiliev, "Energy spectra, sources, and shielding considerations for neutrons generated by a flattening filter-free Clinac," *Medical Physics*, vol. 35, no. 5, p. 1906, 2008.

[30] S. F. Kry, U. Titt, D. Followill, F. Ponisch, O. N. Vassiliev, R. A. White, M. Stovall, and M. Salehpour, "A Monte Carlo model for out-of-field dose calculation from high-energy photon therapy," *Medical Physics*, vol. 34, no. 9, p. 3489, 2007.

[31] R. Barquero, R. Mendez, H. R. Vega-Carrillo, M. P. Iñiguez, and T. M. Edwards, "Neutron spectra and dosimetric features around an 18 MV linac accelerator," *Health physics*, vol. 88, no. 1, pp. 48–58, 2005.

[32] K. Kase, X. Mao, W. Nelson, and J. Liu, "Neutron fluence and energy spectra around the Varian Clinac 2100C/2300C medical accelerator," *Health physics*, 1998.

[33] J. Pena, L. Franco, F. Gómez, a. Iglesias, J. Pardo, and M. Pombar, "Monte Carlo study of Siemens PRIMUS photoneutron production," *Physics in medicine and biology*, vol. 50, pp. 5921–33, December 2005.

[34] R. Katchadourian, "Monte carlo simulations for neutron shielding in radiotherapy bunkers," April 2013.

[35] P. R. Almond, P. J. Biggs, B. Coursey, W. Hanson, M. Saiful Huq, R. Nath, and D. Rogers, "AAPM's TG-51 protocol for clinical reference dosimetry of high-energy photon and electron beams," *Medical Physics Lancaster*, vol. 26, pp. 1847–1870, 1999.

[36] International Standards Organization, "Reference neutron radiations-part 1: Characteristics and methods of production," Tech. Rep. ISO-8529-1, International Organization for Standardization, Geneva, Switzerland, 2001.

[37] M. Hagiwara, T. Sanami, Y. Iwamoto, H. Arakawa, N. Shigyo, N. Mokhov, A. Leveling, D. Boehnlein, V. Kamran, T. Nakamura, *et al.*, "Shielding experiments at high energy accelerators of Fermilab (III): neutron spectrum measurements in intense pulsed neutron fields of the 120-GeV proton facility using a current Bonner sphere technique," *pulse*, vol. 5, p. 9, 2011.

[38] International Commission on Radiological Protection, "Conversion coefficients for use in radiological protection against external radiation," Tech. Rep. ICRP Publication 74, International Organization for Standardization, 1996.

[39] D. Georg, T. Knöös, and B. McClean, "Current status and future perspective of flattening filter free photon beams," *Medical physics*, vol. 38, no. 3, pp. 1280–1293, 2011.

[40] G. Kragl, S. af Wetterstedt, B. Knäusl, M. Lind, P. McCavana, T. Knöös, B. McClean, and D. Georg, "Dosimetric characteristics of 6 and 10MV unflattened photon beams," *Radiotherapy and Oncology*, vol. 93, no. 1, pp. 141–146, 2009.

[41] J. Cashmore, "The characterization of unflattened photon beams from a 6 MV linear accelerator," *Physics in medicine and biology*, vol. 53, no. 7, p. 1933, 2008.

[42] U. Titt, O. Vassiliev, F. Pönisch, L. Dong, H. Liu, and R. Mohan, "A flattening filter free photon treatment concept evaluation with Monte Carlo," *Medical physics*, vol. 33, no. 6, pp. 1595–1602, 2006.

[43] National Council on Radiation Protection and Measurements, "Structural shielding design and evaluation for megavoltage x- and gamma-ray radiotherapy facilities," tech. rep., NCRP Report No. 151, 2005.